学位論文

Highly Sensitive and Point-Measurement Laser Spectroscopy of High Enthalpy Flow

（高エンタルピー気流の高感度および点計測レーザー分光計測）

2012 年度

東京大学新領域創成科学研究科

先端エネルギー工学専攻

野村　哲史

Acknowledgments

First I offer my sincerest appreciation to my supervisor, Prof. Kimiya Komurasaki. He gave me helpful advice and supported my thesis. I'm also pleased that Prof. Yoshihiro Arakawa gave me helpful comments and suggestions for my work. Associate Prof. Hiroyuki Koizumi gave me specific advice about spectroscopic experiment. I appreciate his kind help.

Dr. Georg Herdrich kindly invited me to his research group at IRS and I could spend a really precious time. Dr. Stefan Loehle and Dipl.-Ing. Thomas Marynowski supported my experiments. The experience in Germany was very impressive and interesting. I express here a deep appreciation to all members in IRS.

Dr. Kazuhisa Fujita and Dr. Hiroki Takayanagi gave me a chance to work at the 750 kW arc-heated wind tunnel of JAXA. I would like to thank them all.

I'm pleased to have a nice atmosphere in my research with laboratory members. The discussion with Mr. Cho and Mr. Yamagishi helped my work.

And Mr. Kaneko, Mr. Ito and Mr. Nako also helped my experiments as members in the same research group.

I express my best appreciation to my family.

Contents

List of Figure

List of Table

Nomenclature

A	=	Einstein's A constant
B	=	Einstein's B constant
c	=	speed of light
d	=	diameter
g	=	statistic weight
h	=	Plank's constant
K	=	integrated absorption coefficient
K_G	=	Dale-Gladstone constant
Kn	=	Knudsen number
k	=	absorption coefficient
$\mathbf{k}$	=	wave vector
k_B	=	Boltzmann constant
M	=	molar mass
m	=	atomic mass
N	=	number density
n	=	refraction index
P	=	power
p	=	pressure
Q	=	quenching rate
R	=	mirror reflectivity, relaxation rate
r	=	radius
S	=	saturation intensity
T	=	temperature
t	=	time, thickness
v	=	velocity
$\mathbf{v}$	=	velocity vector
α	=	correction factor
β	=	sweeping speed of laser frequency
ϕ	=	A/(A+Q)
λ	=	wavelength

λ_{mean}	=	mean free path
ν	=	frequency
ρ	=	density
τ	=	time constant
ω	=	angular velocity

Subscripts

BL	=	boundary layer
cs	=	cross-beam saturated
D	=	Doppler
e	=	electron
ex	=	excitation
L	=	Lorentz
i	=	*i*-state
j	=	*j*-state
p	=	probe, probable
RD	=	ring-down
rot	=	rotational
s	=	saturated
t	=	transmitted
tot	=	total
tr	=	translational
vib	=	vibrational
1	=	upstream of shock wave
2	=	downstream of shock wave

Superscripts

0	=	without absorber

Chapter 1 INTRODUCTION

1.1 Simulation of Reentry Condition on the Ground and Plasma Diagnosis

Aerodynamic heating at reentry to the Earth's atmosphere has been investigated experimentally and numerically for sample return missions and return of a transfer vehicle. In the experimental investigation, reentry conditions have been reproduced on the ground by using high enthalpy flow generators, such as shock tubes, shock tunnels and plasma wind tunnels. For a study of radiative heating and chemical reaction, the shock tubes are used[1,2]. For a study of convective heat transfer and aerodynamic force under high temperature condition, the shock tunnels are used[3,4]. The operation time is limited to a few milliseconds, however relatively high enthalpy and stagnation pressure can be achieved with low cost, compared to other facilities. For the developments of heat shields which needs long operation time (1 to 100 s), plasma wind tunnels are used. Arc-heated plasma flow can achieve high heating rate and inductively heated plasma flow is used for the investigation which need a clean flow, such as evaluations of wall catalytic effect. Although it is difficult to exactly reproduce the reentry condition with one ground test facility, these facilities cover their weakness each other and the reentry technology has been developed.

For detailed understanding of heating mechanism and flow properties, high enthalpy flow diagnosis is of importance. The plasma flow is thermally and chemically nonequilibrium and unrevealed effects are still remaining. For modeling of the nonequilibrium flow, detailed characterization of internal energy is necessary. With a development in the optical technologies, optical diagnosis is increasingly developed. Spectroscopic measurements give us information on the internal energy distribution and help us to figure out the nonequilibrium of plasma. Mainly three spectroscopic methods have been applied to the plasma wind tunnel flow, emission spectroscopy, laser-induced fluorescence (LIF) and laser absorption spectroscopy (LAS). Each measurement has advantage and disadvantage, and it is difficult to completely figure out the nonequilibrium plasma only with one method.

1.2 Application of Emission Spectroscopy to High Enthalpy Wind Tunnels

Emission spectroscopy is used to access to translational, rotational, vibrational and electronic excitation temperatures by Boltzmann plot or molecular spectra fitting method using a radiation code such as NEQAIR85[5], NEQAIR96[6], SPRADIAN[7], SPRADIAN2[8], SPRADIAN07[9–11] and PARADE[12].

These codes were originally developed for the prediction of radiative heating. In a numerical simulation, the spectra are predicted as a function of different modes of temperatures, and absolute radiative heating rate is estimated. In contrast, in emission spectroscopy, the spectra are measured and the temperatures are estimated by fitting the measured spectra by simulated one. This emission spectroscopic measurement was applied to inductively heated plasma and temperatures were deduced successfully[8,13]. In arc-heated plasma flow the measured spectra was not fitted well because of its strong thermo chemical nonequilirium, and other spectroscopic thermometry is required. Specific molecular spectra, for instance, H, N_2^+, and NO were also investigated[14,15]. The works of plasma flow diagnosis by emission spectroscopy are summarized in Table 1.1. Although emission spectroscopy has been employed as a powerful tool to obtain molecular spectra and intensity of atomic line spectra or to identify the chemical composition, its wavelength resolution is limited to sub-nanometer. In plasma wind tunnel flow the atomic line broadening is in the order of picometer and can't be resolved by emission spectroscopy. For the evaluation of atomic line broadening the narrow band laser spectroscopy is required.

Table 1.1 Summary of emission spectroscopy for plasma wind tunnels and shock tubes measurements.

Author	Wind tunnel Target	Key words	Reference
Fujita, K.	ICP Overall spectra (N_2, N_2^+, NO)	SPRADIAN	8,13
Takama, Y.	ICP H_2, Balmer H_β, Fulcher-α	Translational-Rotational nonequilibrium	14
Mizuno, M.	ICP Ar, O I	Actinometry	16
Kihara, H.	arc CN, C_2 swan	Spallation particles from ablator	17
Cohen, L.M.	ICP N_2^+, first negative system	Thermal nonequilibrium	15
Hirakawa, M.	arc (20kW class) N_2^+	Catalytic effect	18
Park, C.	shock tube	Two-temperature kinetic model	19
Filippis, F.	arc (SCIROCCO) NO (*A*-*X*)	Nonequilibrium	20
Marschall, J.	ICP, Arc N_2^+	Interaction with UHTC	21

1.3 Application of Laser Absorption Spectroscopy to High Enthalpy Wind Tunnels and Its Problems

Laser absorption spectroscopy (LAS) is a powerful tool to resolve an atomic absorption profile. An external cavity diode laser (ECDL) whose spectral width is usually less than 1 MHz enables to resolve a very narrow spectrum (sub-MHz). In the previous work, LAS has been applied to measure translational temperature, flow velocity and number density of absorbing particles in argon and oxygen plasma[22,23]. Furthermore, a combination with other measurement enabled more detailed measurements. For instance, specific heat ratio was deduced experimentally in combination with pitot probe measurement[24], and population temperature was also estimated in combination with LIF[25]. In the air plasma flow, on the other hand, currently there is no successful work of absorption measurements. Even at a 60 MW arc heater (IHF) of NASA Ames Research Center, the absorption signal has not been obtained in the flow[26]. The reason for this is the fact that the input energy is consumed in dissociation of molecular nitrogen and number density of excited state atoms is lower than the detectable limit of LAS. Another reason is the phenomenon that the thermal energy at the plenum is converted into the kinetic energy though a nozzle and the electronic excitation in the flow is low. Instead, they measured inside the arc heater and estimated population temperature[26]. The deviation from thermal equilibrium, however, occurs though the nozzle and it is quite difficult to estimate the flow condition from the plenum conditions. Thus, for absorption measurement in the flow, enhancement of the LAS's sensitivity is necessary. In this thesis, the highly sensitive laser absorption spectroscopy is applied to an arc-heated plasma wind tunnel equipped in Japan Aerospace Exploration Agency (JAXA) to observe the absorption of atomic oxygen in the air plasma flow.

Table 1.2 Summary of LAS for high enthalpy flow diagnosis.

Author	Wind tunnel	Target	Parameter	Reference
Kim, S.	IHF(segmented arc)	O I, N I, Ar, Cu	N, T_{pop}	26
Mohamed, A.	Hyper sonic	NO	T	27
Matsui, M	Arc, ICP	Ar, O I	N, T_{tr}, V	28

Another problem in LAS is spatial resolution. LAS is one of line-of-sight measurements. For spatially resolved measurement, data reconstruction method is required. In plasma wind tunnel measurements, the flow has an axisymmetric distribution and Abel inversion is often used. However Abel inversion can't be applied in some cases. In shock layer measurements, for instance, the flow

has a velocity component in the radial direction as shown in Figure 1.1. Until the laser propagation reaches the center line, the absorption shifts to the blue side and in the later region to the red side by Doppler shift effect. The resultant line-integrated absorption signal, which is the convolution of blue shifted and red shifted profiles, shows the wider profile than the true profile and yields the overestimated temperature. Therefore for translational temperature measurement in the shock layer, point-measurement technique is required. In this thesis a novel technique for a point-measurement LAS is developed.

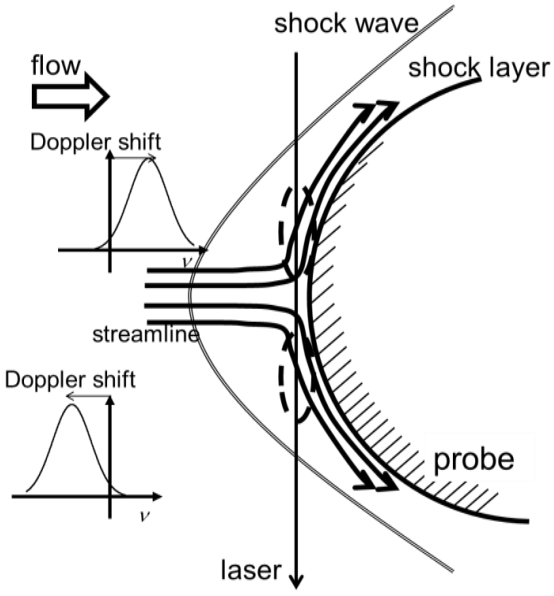

Figure 1.1 Schematic of LAS in a shock layer.

1.4 Application of Laser-Induced Fluorescence to High Enthalpy Wind Tunnels and Its Problems

In plasma wind tunnel measurements, two-photon absorption laser-induced fluorescence (TALIF) is widely used to measure number density of atomic nitrogen[29] and oxygen[30,31]. The advantage of TALIF lies in the accessibility to the ground electronic-excited state and in the possibility of point-measurements. In a plasma wind tunnel flow, most of particles lie in the ground electronic-excited state (ground state), and the ground state atoms' number density are the most important flow properties. In particular, the degree of dissociation of molecular nitrogen is often unknown and experimental investigation is desired to deepen the insight on the flow condition. One

difficulty in number density measurements by TALIF is the evaluation of two-photon excitation cross section. Usually the fluorescence intensity is calibrated by measuring a flow reactor which is either a microwave discharged oxygen plasma[32] or xenon gas[33]. In spite of this difficulty, TALIF is the common technique in number density measurements.

TALIF is also applied for translational temperature measurements. When Doppler broadening is wider than the spectral line width of excitation dye laser, the temperature can be deduced successfully[31,34]. In contrast, when Doppler broadening is comparable with the spectral line width of dye laser, LIF profile is the convolution of laser spectral profile and atomic profile, and it is difficult to deduce Doppler broadening from the LIF profile. In this thesis we focus on the latter case. For resolving the narrow atomic profile, diode laser-induced fluorescence (DLIF) is a powerful tool. The spectral width of ECDL (sub-MHz) is three orders of magnitude narrower than that of dye laser and enables to resolve the line broadening of 0.1 GHz which corresponds to less than 10 K. Although DLIF is an attractive method for translational temperature measurements, in optically thick plasma its fluorescence profile is distorted by the absorption of laser and re-absorption of fluorescence. The detail about this effect is discussed in Chapter 4. In addition, DLIF can't be applied to optically thick shock layer measurements because the laser absorption is shifted to the blue side and the fluorescence re-absorption is shifted to the red side. The detail of this problem is discussed in Chapter 5.

LIF is applied also to the molecular transitions. In arc-heated air plasma rotational temperature of NO molecules was measured[30,35]. In hypersonic wind tunnel air flow O_2 was measured[36]. In these measurements, the required wavelength resolution is not as high as that in translational temperature measurement. Thus the dye laser was effectively employed. Planar LIF was applied to obtain the image of vibrationally excited NO molecules at the shock tunnel[37]. Finally, the LIF measurements in high enthalpy flows are summarized in Table 1.3.

Table 1.3 Summary of LIF measurements in high enthalpy flows.

Author	Wind tunnel	Target	Parameter	Reference
Fletcher, DG.	Arc	N I	N	29
Loele, S.	ICP	O I	N, T_{tr}	31
Takayanagi	Arc	O I, N I	N, T_{tr}	32
Yamada, T.	Segmented Arc	NO	T_{rot}	35
Laufer, G.	Hypersonic wind tunnel	O2	T	36

1.5 Simulation of Entry Condition to Other Planets on the Ground and Plasma Diagnosis

The atmospheric pressure of Mars is low (0.7~0.9 kPa) and the heating condition is not as severe as the Earth's reentry condition. However the atmospheric compositions of Mars are CO_2 and N_2, and radiative heating and wall catalytic recombination are different from those in the reentry condition. In particular, radiation from carbonaceous molecules, C_2, CN, CO and CO^+ is of importance[38]. There are a number of problems to be experimentally investigated. While, it is difficult to generate CO2 plasma because of the fact that CO damages the vacuum pump and CO_2 is reactant gas. For deactivation of the exhaust gas which includes CO, a large amount of N_2 gas is fed at the end of chamber. Hence a vacuum system with a high pumping speed is required. Furthermore, when arc-heated plasma generators are used with CO_2, carbon is accumulated on the electrode and disturbs the stable discharge. In spite of these difficulties, a number of ground facilities are being developed in Europe. The facilities in Europe are listed in a review article[39]. In Japan, Aichi Institute of Technology has a Huels type arc heater[40] for CO_2 plasma generation. Recently the entry condition to Mars is increasingly investigated in the world. The plasma wind tunnels for Mars entry conditions are summarized in Table 1.4.

Table 1.4 Summary of CO_2 plasma wind tunnels.

Country	Plasma wind tunnel	Reference
Japan	Huels arc	40
Germany	IPG3 (ICP)	41
Germany	L2K (Huels arc)	42
France	SCIROCCO (segmented arc)	43
France	SR1 (constrictor arc)	44
USA	HYMETS (segmented arc)	45

Optical diagnosis of CO2 plasma is also being developed. Emission spectroscopy is the most widely used. Vibrational temperature was obtained by analyzing C_2 SWAN band which shows the highest intensity in the spectrum in the free stream[40]. Chemical reaction in CO_2 plasma was also investigated at RF plasma torch by measuring the emission at four different location[46]. DLIF was also applied to measure atomic oxygen and velocity and temperature were obtained[47]. LAS was applied to measure the absorption of atomic oxygen in CO_2 plasma at an inductively heated plasma

generator at IRS(Institute of space systems). The absorption signal is shown in Figure 1.2.

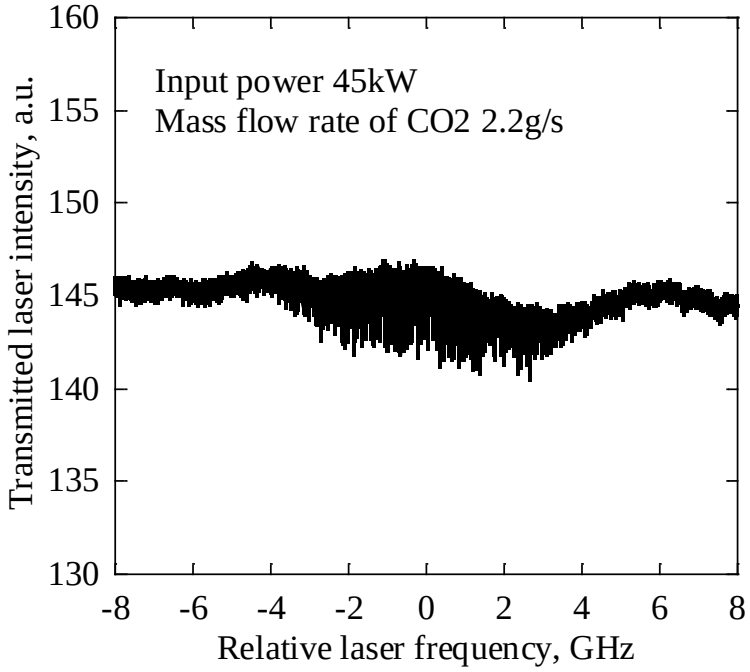

Figure 1.2 Absorption signal of atomic oxygen in CO_2 plasma. (Input power 45 kW, mass flow rate of CO_2 2.2 g/s)

Figure 1.3 shows the absorbance profile with Gaussian fitting curve. The peak absorbance is about 0.02. Also in CO2 plasma, the electric excitation is not high enough to have a sufficient absorption signal. It is noteworthy that sensitivity enhancement of LAS is required also for atomic oxygen measurement in CO_2 plasma flows.

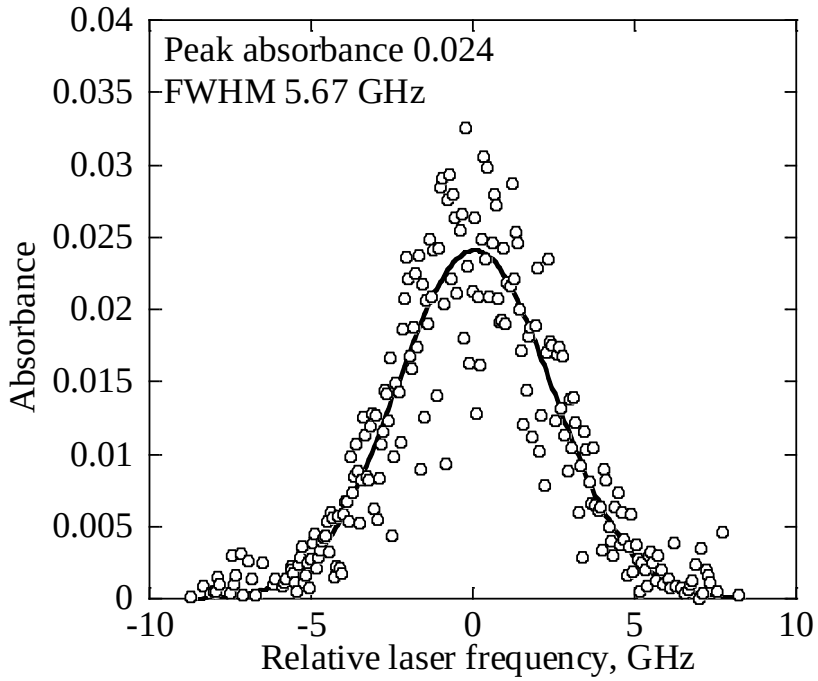

Figure 1.3 Absorbance of atomic oxygen in CO_2 plasma with Gaussian fitting.

The entry condition to Venus and Titan are also investigated. At the entry to Venus, the high atmospheric pressure (9 MPa) leads to much more severe heating than that in Mars entry condition. It is difficult to achieve such high stagnation pressure with a plasma wind tunnel. The number of experimental research is limited. Currently a laser driven CO_2 plasma generator is under development. At the entry to Titan, the entry velocity is moderate; however the radiative heating is severe. The investigations of optical diagnosis at the plasma wind tunnels and shock tubes which simulate the entry condition to Mars, Venus and Titan, are summarized in Table 1.5.

Table 1.5 Summary of investigation on entry to other planets.

Author	Planets	Diagnostics	Target	Reference
G. Herdrich	Mars, Venus	OES	ICP	[41]
V. Lago	Mars, Titan	OES	Arc	[44]
S., Mazouffre	Mars	DLIF	Arc, O I(777)	[47]
M. Playez	Titan	OES	ICP	[48]
A.M., Brandis	Titan	OES	Shock tube	[49]

1.6 Objectives

Although some properties in free stream of plasma wind tunnels have been revealed by spectroscopic measurements, diagnostics of translational temperature is not established yet. Objectives of this thesis are 1) to measure the absorption of atomic oxygen in the arc-heated air plasma flow, 2) to apply DLIF to optically thick plasma in combination with LAS and 3) to develop a novel technique for translational temperature measurement in the shock layer. The uncertainty of 5% is targeted to show an advantage over existing estimation methods.

1) Observation of the atomic oxygen absorption in the arc-heated air plasma flow

Cavity enhanced absorption spectroscopy is applied to measure atomic oxygen at 750 kW arc-heated plasma wind tunnel.

2) Extension of applicable region in LIF spectroscopy to optically thick plasma in combination with LAS

The absorption of laser, re-absorption of fluorescence and saturation broadening are corrected in combination with LAS.

3) Development of a novel technique for the access to translational temperature in the shock layer

For point measurement of translational temperature, cross-beam saturated absorption spectroscopy is developed and applied to shock layer measurement.

Chapter 2 PRINCIPLE OF ATOMIC LINE BROADENINGS AND NON-LINEAR ABSORPTION

2.1 Homogeneous and Inhomogeneous Broadenings

The profiles of atomic fluorescence and absorption are broadened by different kinds of mechanism such as thermal motion of atoms, pressure, electric field and magnetic field. The spectra are not monochromatic. When the probability of transition is equal for all atoms, the broadening of this transition profile is called as the homogeneous broadening. The broadenings oriented by pressure, electric field and magnetic field are the homogeneous broadenings. On the other hand, when the transition probability is dependent on atoms, the spectral width is termed as an inhomogeneous broadening. Only Doppler broadening which is oriented by thermal motion belongs to the inhomogeneous broadening. The homogeneous and inhomogeneous broadenings are respectively expressed by Lorentz and Gaussian functions. Generally the profile is a convolution of these broadenings and represented by a Voigt function. By resolving each broadenings, physical parameters which induce each broadenings are obtained. Translational temperature is obtainable by evaluating Doppler broadening. In plasma wind tunnel measurements usually Doppler broadening is larger than other broadenings by three orders of magnitude approximately[50]. Thus the profile is evaluated by a Gaussian function and the translational temperature is deduced from the broadening. In laser spectroscopy, however the intense light source can induce the additional broadening termed as saturation or power broadening. In most application the saturation regime is avoided to have a pure Gaussian profile by using a low intensity laser. In this thesis, however, the saturation effect is intentionally used. Thus the theories of Doppler broadening and saturation broadening are introduced in this chapter. The other broadenings such as collisional broadening, natural broadening and transit-time broadening are well explained in the reference[51]. The broadenings are listed in Table 2.1

Table 2.1 Summary of Broadenings.

Broadening	Origin	Line shape function
Pressure	Collision	Lorentz
Stark	Electric field	Lorentz
Zeeman	Magnetic field	Lorentz

Natural	Finite time of transition	Lorentz
Doppler	Thermal motion of atoms	Gauss

2.2 Doppler Broadening

The absorption frequency of atoms which have a velocity vector, $\mathbf{v} = \{v_x, v_y, v_z\}$ is shifted because of the Doppler effect as

$$\nu = \nu_0 + \frac{1}{2\pi}\mathbf{k}\cdot\mathbf{v}. \tag{2.1}$$

Here ν, ν_0, and $\mathbf{k}$ respectively denote the absorption frequency, center frequency of absorption, and wave vector. When the laser propagates along the x-axis, i.e. $\mathbf{k} = \{k_x, 0, 0\}$, the absorption frequency of the atoms is

$$\nu = \nu_0\left(1 + \frac{v_x}{c}\right), \tag{2.2}$$

where c is the speed of light. In thermal equilibrium state, the number density of atoms with a velocity component of v_x to v_x+dv_x, v_y to v_y+dv_y and v_z to v_z+dv_z is expressed by

$$n_i\left(v_x, v_y, v_z\right)dv_x dv_y dv_z = N_i\left(\frac{1}{\sqrt{\pi}v_p}\right)^3 \exp\left(-\frac{v^2{}_x + v^2{}_y + v^2{}_z}{v^2{}_p}\right)dv_x dv_y dv_z, \tag{2.3}$$

N_i and v_p are the number density on the excited i-state and the most probable velocity. v_p is a function of translational temperature, T_{tr}.

$$v_p = \sqrt{2k_B T_{tr}/m} \tag{2.4}$$

Here k_B and m are the Boltzmann constant and atomic mass, respectively. The number density of atoms with a velocity component between v_x and v_x+dv_x, $n_i(v_x)$ is obtained by integrating Equation (2.3) over v_y and v_z.

$$n_i\left(v_x\right)dv_x = \frac{N_i}{v_p\sqrt{\pi}}\exp\left\{-\left(\frac{v_x}{v_p}\right)^2\right\}dv_x. \tag{2.5}$$

Inserting Equation (2.2) into Equation (2.5), the number density of atoms which absorbs the laser with frequency ν is

$$n_i(\nu)d\nu = N_i \frac{c}{\nu_0 \nu_p \sqrt{\pi}} \exp\left\{-\left(\frac{c(\nu-\nu_0)}{\nu_0 \nu_p}\right)^2\right\} d\nu \quad . \tag{2.6}$$

Absorption coefficient is proportional to number density of absorbing particle. Therefore, the Doppler broaden profile is expressed as

$$k(\nu) = K_i \frac{2\sqrt{\ln 2}}{\sqrt{\pi}\Delta\nu_D} \exp\left\{-\left(\frac{(\nu-\nu_0)}{\Delta\nu_D / 2\sqrt{\ln 2}}\right)^2\right\}. \tag{2.7}$$

Here K_i and $\Delta\nu_D$ are the integrated absorption coefficient and full width at half maximum of the Gaussian profile. Thus $\Delta\nu_D$ is related to T_{tr} as follows.

$$\Delta\nu_D = \frac{2\nu_0\sqrt{\ln 2}}{c}\sqrt{\frac{2k_{\mathrm{B}}T_{\mathrm{tr}}}{m}} \tag{2.8}$$

In the application of plasma wind tunnel measurement, $\Delta\nu_D$ ranges from 1 GHz to 10 GHz. This corresponds to the wavelength of 2~20 pico meter. Hence, it is difficult to spectrally resolve a Doppler broadened profile with a spectrometer. In laser spectroscopy if the spectral width of light source is much narrower than $\Delta\nu_D$ it is possible to evaluate the broadening accurately. In systems where two laser beams counter-propagate or cross with an angle, the aforementioned description is not valid. The details of these cases are shown in Chapter 3 and 5.

Uncertainty analysis of translational temperature measurements by LAS was discussed by Matsui[50]. The uncertainty of T_{tr} is related to the uncertainty of k by

$$\frac{\Delta T_{\mathrm{tr}}}{T_{\mathrm{tr}}} = 2\frac{\Delta(\Delta\nu_D)}{\Delta\nu_D} \cong 2\frac{\Delta k}{k}\,. \tag{2.9}$$

In this thesis, temperature measurements by LAS are performed with the uncertainty of 5%, and the error bar represents this uncertainty.

2.3 Convolution of Homogeneous and Inhomogeneous Broadenings

In general, the profile is a convolution of homogeneous and inhomogeneous broadened profiles. The total absorption coefficient is expressed by

$$k(\nu) = K_i \frac{\sqrt{\ln 2}}{\pi^{3/2}} \frac{\Delta\nu_L}{\Delta\nu_D} \int_{-\infty}^{\infty} \frac{\exp\left\{-(\nu_\xi - \nu_0)^2 / \left(\Delta\nu_D / 2\sqrt{\ln 2}\right)^2\right\} d\nu_\xi}{(\nu - \nu_\xi)^2 + (\Delta\nu_L / 2)^2}\,. \tag{2.10}$$

This function is called as a Voigt function. This cannot be expressed in closed form and has to be

calculated numerically. A number of investigations on the Voigt function have been published and pseudo-Voigt function has been developed for a simple calculation with closed form[52,53]. The Voigt function is closely related to a complex error function[54,55].

2.4 Non-linear Absorption

When a laser frequency matches with the absorption line between two energy levels, the lower state atoms are excited to the upper state. If the laser intensity is substantially intense, number density on the lower state deletes and absorption coefficient is underestimated. This effect is explained either by optical Bloch equation which is based on quantum theory or by the rate equations. In this thesis, saturation is explained by using the rate equations. Furthermore, saturation broadens the absorption profile. This broadening is called as saturation broadening or power broadening. First, the saturation of number density in two different systems is introduced with rate equations. Next, saturation broadening in homogeneously and inhomogeneously broadened profile are explained.

2.4.1 Closed two-level system

First, simple system is considered, in which only two energy levels exist and there is no transition to other levels as shown in Figure 2.1. The rate equation is expressed by

$$\frac{dN_1}{dt} = -\frac{dN_2}{dt} = -B_{12}\rho N_1 - R_1 N_1 + B_{12}\rho N_2 + R_2 N_2 \quad , \tag{2.11}$$

assuming g_1=g_2=1. B_{12}, ρ and R respectively denote the Einstein's constant, spectral energy density and relaxation rate. g_1 and g_2 are the statistical weight. In a steady state,

$$\frac{dN_i}{dt} = 0 \quad . \tag{2.12}$$

By solving Equations (2.11) and (2.12), the number density of lower state atoms are expressed as

$$N_1 = N_{\text{tot}} \frac{1 + \left(R_2 / B_{12}\rho\right)}{2 + \left(\dfrac{R_1 + R_2}{B_{12}\rho}\right)} \quad , \tag{2.13}$$

where N_{tot} is the total number density in the system,

$$N_{\text{tot}} = N_1 + N_2 \quad . \tag{2.14}$$

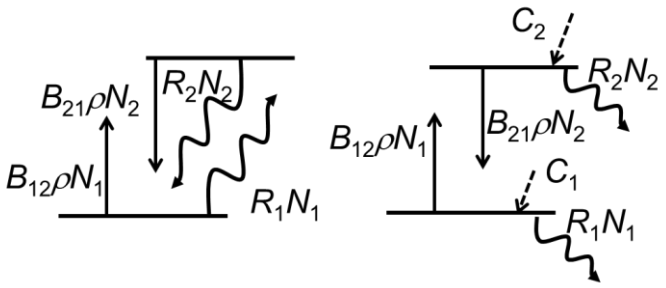

Figure 2.1 Closed (Left) and open (Right) two-level systems.

When there is no radiation field (ρ=0) in the system,

$$N_{i0} = \left(1 - \frac{R_i}{R_1 + R_2}\right) N_{\text{tot}}, (i=1,2). \tag{2.15}$$

N_{i0} is the number density under the no radiation field. From Equations (2.13) and (2.15) the difference of number density between two levels is deduced as

$$\Delta N = \frac{\Delta N_0}{1+S}, \tag{2.16}$$

here, S is the saturation parameter and expressed as

$$S = \frac{B_{12}\rho}{(R_1 + R_2)/2}. \tag{2.17}$$

Here, $\Delta N=N_1-N_2$ and $\Delta N_0=N_{10}-N_{20}$. S is the ratio of the probability of induced absorption to the averaged relaxation rate. When $B_{12}\rho$ is larger than $(R_1+R_2)/2$, the number density difference ΔN decreases and in the limit of S to the infinity, N_1 is equal to N_2. The closed two-level system is realized by transitions without hyperfine structures[51].

2.4.2 Open two-level system

In open two-level system, the population of the systems from other levels and the depopulation towards other levels have to be taken into considered as illustrated in Figure 2.1. The rate equation is expressed as

$$\frac{dN_i}{dt} = B_{12}\rho(N_t - 2N_i) - R_i N_i + C_i, \tag{2.18}$$

where R_i is the total relaxation rate which includes spontaneous emission from i state. C_i is the population rate into i state.

$$C_i = \sum_k R_{ki} N_k + D_i \tag{2.19}$$

D_i is the diffusion rate. In a stationary state, the saturated number density difference is expressed with the unsaturated number density difference as follows.

$$\Delta N = \frac{\Delta N_0}{1 + B_{12}\rho\left(1/R_1 + 1/R_2\right)}. \tag{2.20}$$

Now the saturation parameter S is

$$S = \frac{B_{12}\rho}{R_1 R_2 /\left(R_1 + R_2\right)}. \tag{2.21}$$

The difference of S between closed system and open system is the relaxation rate in the denominator. By introducing the average relaxation rate, $\bar{R}$ for both systems saturation parameter can be expressed by

$$S = \frac{B_{12}\rho}{\bar{R}}. \tag{2.22}$$

The more complex system with open multiple levels was also investigated[56]. In any cases saturation parameter can be expressed by Equation (2.22).

2.4.3 Saturation broadening in a homogeneously broadened profile

Saturation broadens the absorption profiles. This is called as saturation broadening or power broadening. In homogeneous line profiles, the saturation intensity is a function of ν and follows the Lorentzian function as

$$S(\nu) = S_0 \frac{\Delta\nu_L^2}{(\nu - \nu_0)^2 + \Delta\nu_L^2}, \tag{2.23}$$

where S_0=S(0). The intensity decrease dI is expressed as

$$dI = h\nu B_{12}\rho \frac{\Delta N_0}{1+S}. \tag{2.24}$$

Inserting Equation (2.23) into Equation(2.24), the saturated absorption coefficient of homogeneously broadened profile is expressed by

$$k_s(\nu) = k(\nu)\frac{1}{1+S(\nu)}. \tag{2.25}$$

FWHM of the saturated profile is wider than unsaturated broadening.

$$\Delta\nu_{Ls} = \Delta\nu_L\sqrt{1+S_0}. \tag{2.26}$$

2.4.4 Saturation broadening in an inhomogeneously broadened profile

In the conventional theory, the saturated absorption coefficient of inhomogeneously broadened profile is expressed as

$$k(\nu)=K_i\frac{\sqrt{\ln 2}}{\pi^{3/2}}\frac{\Delta\nu_L}{\Delta\nu_D}\int_{-\infty}^{\infty}\frac{\exp\left\{-\left(\nu_\xi-\nu_0\right)^2/\left(\Delta\nu_D/2\sqrt{\ln 2}\right)^2\right\}d\nu_\xi}{\left(\nu-\nu_\xi\right)^2+\left(\Delta\nu_L\sqrt{1+S_0}/2\right)^2}. \tag{2.27}$$

When the inhomogeneous broadening is much more dominant than the homogeneous broadening, the numerator does not vary much and can be taken out of integration. The denominator can be integrated analytically and k_s is simply related with k. The following expression shows that the broadening doesn't vary with increasing S_0. Equation (2.28) infers that the saturated profile's broadening is identical to that of the non-saturated profile.

$$k_s(\nu)=k(\nu)\frac{1}{\sqrt{1+S_0}} \tag{2.28}$$

Matsui found that even in the inhomogeneously broadened profile broadening of the saturated profile is wider than that of non-saturated profile, and modified the line shape function of saturated absorption profile[50]. As shown in Equation (2.29) the saturation intensity is a function of Lorentzian broadening and when the pressure broadening is dominant among the homogeneous broadenings, I_s is expressed as

$$I_s=\frac{2\pi^2 h\nu^3 N_i\bar{v}\sigma}{\phi c^2}. \tag{2.29}$$

Here σ and $\bar{v}$ are the collision cross section and Root-mean-squire velocity. In thermal equilibrium state, $\bar{v}$ is described as

$$\bar{v}=\sqrt{\frac{3k_{\mathrm{B}}T_{\mathrm{tr}}}{m}}. \tag{2.30}$$

As shown in Equation (2.2), the atoms whose absorption frequency is far away from the center have a large velocity component in the lase r propagation direction as follows.

$$v_x=c\left(\frac{\nu}{\nu_0}-1\right) \tag{2.31}$$

As to the atoms which absorb the laser with frequency, ν, the frequency-selective root-mean squire velocity is different from $\bar{v}$ for overall atoms. Frequency-selective $\bar{v}$ is the function of absorption frequency.

$$\bar{v}(\nu)=\sqrt{\left(\nu-\nu_0\right)^2\frac{c^2}{\nu_0^2}+\frac{2k_{\mathrm{B}}T_{\mathrm{tr}}}{m}} \tag{2.32}$$

The modified saturation intensity $I_s(\nu)$is expressed as

$$I_s(\nu) = I_s \sqrt{\frac{8\ln 2}{3}\frac{(\nu-\nu_0)^2}{\Delta\nu_D{}^2} + \frac{2}{3}} \tag{2.33}$$

The saturation intensity around the profile's wing is higher than that near the absorption center line. The saturated absorption coefficient is written as follows.

$$k_s = \frac{\sqrt{\ln 2}}{\pi^{3/2}}\frac{\Delta\nu_L}{\Delta\nu_D}\int_{-\infty}^{\infty}\frac{\exp\left\{-(\nu_\xi-\nu_0)^2/\left(\Delta\nu_D/2\sqrt{\ln 2}\right)^2\right\}d\nu_\xi}{(\nu-\nu_\xi)^2+\left(\Delta\nu_L\sqrt{1+I/I_s(\nu)}/2\right)^2} \tag{2.34}$$

This function shows that the profile is broadened by increasing I/I_s.

Chapter 3 ABSORPTION MEASUREMENT IN AN ARC-HEATED PLASMA WIND TUNNEL BY CAVITY ENHANCED ABSORPTION SPECTROSCOPY

Currently there is no successful work of LAS measurement in any arc-heated air plasma flow except for the absorption of copper which comes from the electrode erosion. This is because absorbance between two excitation states is quite small because of its low electric excitation. Cavity enhanced absorption spectroscopy (CEAS) was applied to an arc-heated plasma wind tunnel at Japan Aerospace Exploration Agency (JAXA) and the absorption of atomic oxygen was observed. To our best knowledge this is the first demonstration of the absorption measurement in the arc-heated air plasma flow.

3.1 Sensitivity Enhancement of LAS

According to the Beer-Lambert law, the absorption, *dI*, is proportional to the optical length, *dx* as shown in Eq.(3.1).

$$dI = -kIdx \tag{3.1}$$

Here *k* is the absorption coefficient. Integration of the absorption coefficient over the optical length $\int kdx = -\ln(I/I_0)$ is termed as absorbance. The minimum detectable absorbance is determined by minimum detectable (I_0-I) and usually the minimum detectable absorbance is about 0.01. The sensitivity of LAS is enhanced by amplifying *dx*, using an optical cavity. There are a number of techniques of highly sensitive LAS which use the optical cavity, such as cavity ring-down spectroscopy (CRDS)[57,58], integrated cavity output spectroscopy (ICOS), cavity enhanced absorption spectroscopy (CEAS)[59] and noise-immune cavity-enhanced optical heterodyne molecular spectroscopy (NICE-OHMS)[60,61]. In this work, CEAS is adopted because CEAS is less equipped than other techniques. It should be noted that sensitivity enhancement is achieved also by a signal-to-noise ratio improvement. Wavelength modulation spectroscopy (WMS) and frequency modulation spectroscopy (FMS)[62] are also well developed. Recently the combination of cavity method and modulation method was also reported. In the following section CEAS is explained in detail. The other techniques are well summarized in the references[63,64].

3.2 Practical Theory of Optical Cavity and CEAS

3.2.1 Fabry-Perot cavity

In this work a pair of highly reflective mirrors was used, which is known as a Fabry-Perot cavity. The laser transmittance from the cavity is a function of laser wavelength. In the Fabry-Perot cavity's theory, the propagation time of the light inside the cavity is not taken into account. The transmitted intensity I_t can be simply described as a function of laser wavelength λ as shown in Equation (3.2). This is termed as an Airy function.

$$\frac{I_t}{I_0} = \frac{(1-R)^2}{(1-R)^2 + 4R\sin^2\left(\frac{L}{\lambda}\pi\right)} \tag{3.2}$$

I_0, R, c, and L respectively denote the incident laser intensity, reflectivity, speed of light, and cavity length. The higher the reflectivity is the sharper the profile is. The detector's bandwidth has to be set carefully. The transmitted laser intensity is shown in Figure 3.1.

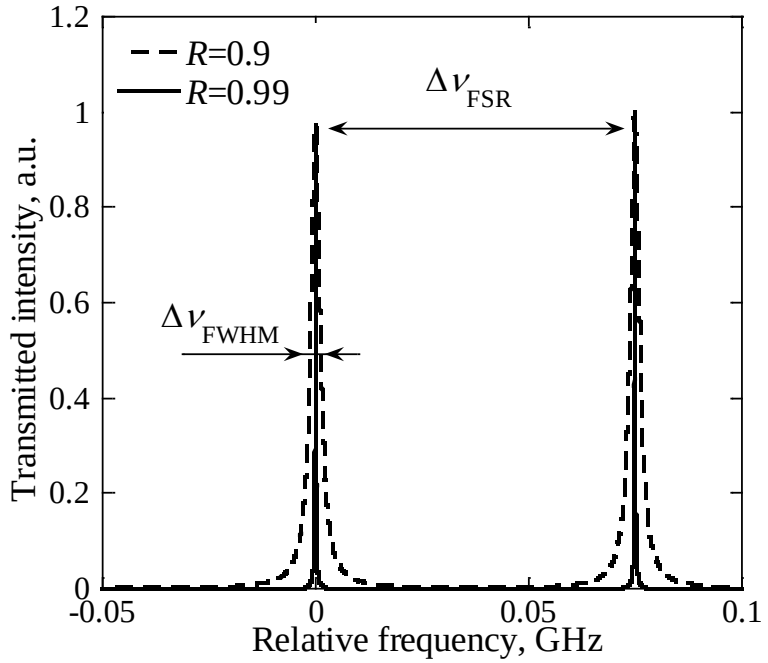

Figure 3.1 Transmitted laser intensity as a function of frequency.

In trace gas measurement, the cavity which has more than two mirrors are used with a V-shape configuration[65,66] to improve the sensitivity at low cost. In plasma wind tunnel measurement,

however, one has to build up the optical cavity in a limited space and the complex setup is not preferable. Thus for simplicity the typical Fabry-Perot cavity is employed in this work.

3.2.2 Tuning to resonance

When mirror reflectivity is high, the resonance bandwidth is very narrow. For instance, when R and L are respectively 0.999 and 1 m, full width at half maximum (FWHM) of the resonance profile, $\Delta\nu_{\mathrm{FWHM}}$ is 48 kHz and free spectral range (FSR), $\Delta\nu_{\mathrm{FRS}}$ is 150 MHz. Meanwhile the line width of the probe laser is from 100 kHz to 1 MHz. Thus the challenge lies in tuning the laser frequency to the resonance. In this paper the accidental matching is employed by sweeping the laser frequency across the absorption line. In some works an active locking system is employed using the Pound-Drever-Hall (PDH) method[67,68]. It is reported that the active locking system enables more sensitive measurement than passive locking system however this system requires a complex setup and expensive optics.

3.2.3 Resonance mode

In this work, the cavity was aligned for a resonance on a longitude mode. When the laser light repeats the reflective propagation on the same pass, the transmitted laser intensity shows the longitude mode (or on-axis mode) resonance. In this case the transmitted intensity profile can be expressed with Equation (3.2). In contrast, when the cavity is misaligned because of external turbulence, the laser does not repeat the same reflection inside the cavity and the transmitted intensity shows a transverse mode (or off-axis mode, higher-order mode) resonance. The transmitted laser intensity of these two modes is shown in Figure 3.2. Figure 3.2 (a) is the resonance signal on the longitude mode. When the cavity is misaligned the transverse mode signal appears as shown in Figure 3.2 (b). In the case of more misaligned cavity, the transmitted intensity becomes low and the resonance signal on the higher order mode increases as shown in Figure 3.2 (c) and (d). The relationship between misalignment degree and transmitted intensity was discussed by Anderson[69], considering the misalignment such as transverse position, angular tilt, waist size, and waist axial position. The peak intensity of the longitude mode resonance is higher than that of the transverse mode resonance, and to achieve a high signal-to-noise ratio the longitude mode is preferable. Nevertheless, the measurement environment at the plasma wind tunnel is harsh because of a mechanical vibration from high-pressure cooling water, vacuum pumps, and other facilities. Under such vibrating condition, the optical cavity which is built up for the on-axis mode is misaligned with different kinds of degree and the transmitted intensity shows the complex mixture of different order resonance. This is the difficulty in CEAS measurements in plasma wind tunnels.

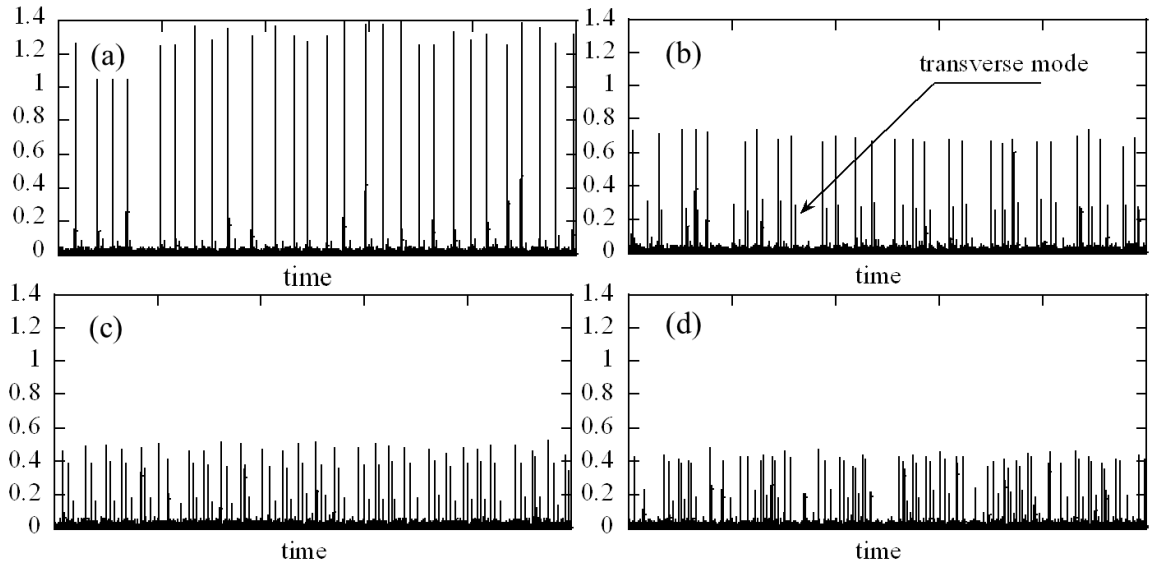

Figure 3.2 Transmitted laser intensity on the longitude mode and transverse mode. The cavity is aligned only for the longitude mode in (a). The cavity is misaligned in (b) and the degree of misalignment is increased in (c) and (d).

3.2.4 Rapid sweep of laser frequency

When the laser frequency is swept more rapidly than a mechanical vibration, the transverse mode can be eliminated. At the rapid sweeping rate , however, the transmitted profile departs from the Airy function[70,71] and transmitted intensity gets lower. As mentioned above, in Airy function the laser frequency is unchanged until the laser transmits the cavity completely. At the rapid sweeping rate, however the frequency change during the laser propagation becomes substantial as the sweeping speed increases. Thus Airy function is not valid and the resonance profile is described by Equations (3.3) and (3.4)[70]. Figure 3.3 shows the simulated resonance profiles with various sweeping speeds and Figure 3.4 shows the experimental data of resonance signal with the simulated curve. The peak intensity decreases as the speed increases and the ringing appears at the tail. In plasma wind tunnel measurements, the transmitted laser intensity has to be high enough to be distinguished from the self-emission from the plasma. The sweeping speed has to be set carefully. It is noteworthy that the ringing profile on the tail can be used to measure the mirror reflectivity[71,72].

$$A_{\text{out}}(t,z) = (1-R)A_{in}(t,z)\sum_{n=0}^{\infty} R^n \exp(i\Phi_n) \tag{3.3}$$

where

$$\Phi_n = 2\pi\nu\left\{n\left[\frac{2L}{c}+\left(2t-2\frac{z+L}{c}\right)\frac{v}{c}\right]+n^2\frac{2L}{c}\frac{v}{c}\right\}. \tag{3.4}$$

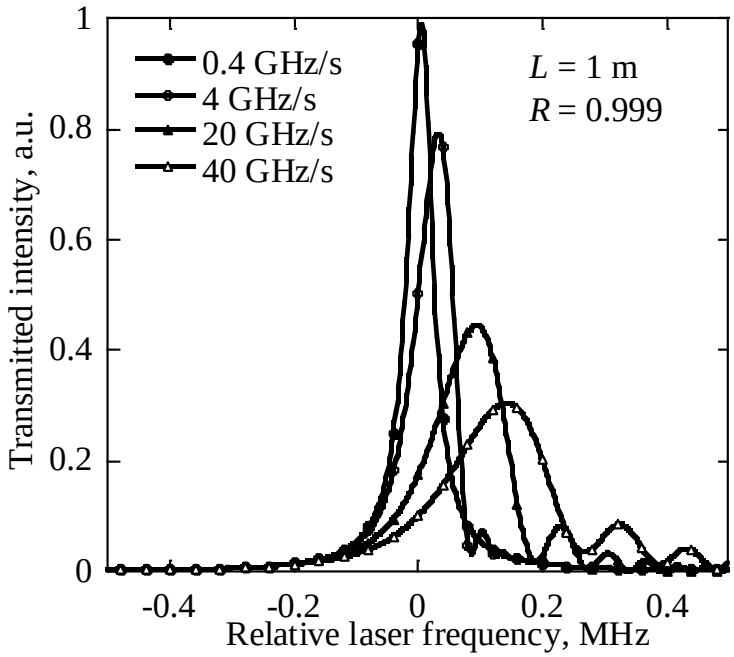

Figure 3.3 Simulated resonance profiles with varying sweeping speed of laser frequency.

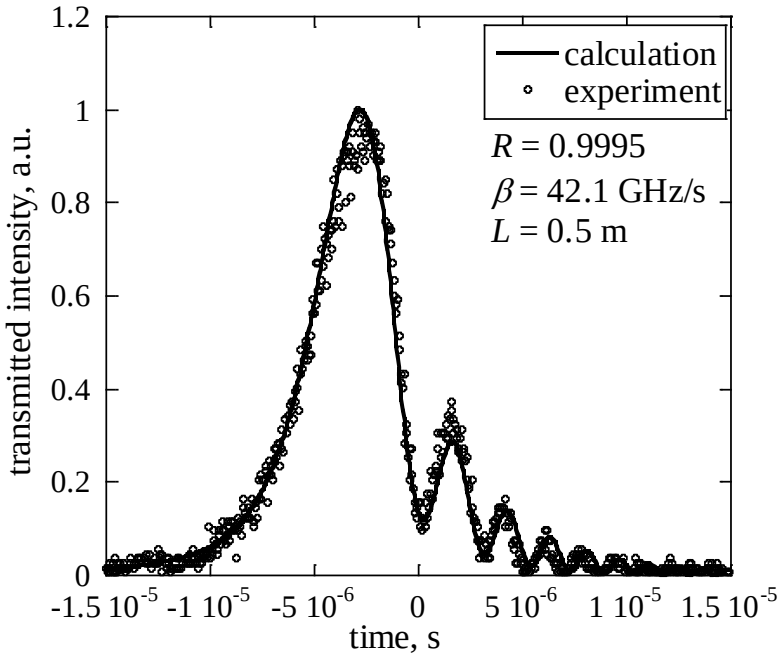

Figure 3.4 Experimental data of resonance signal at rapid sweeping with theoretical curve.

3.2.5 Reflectivity measurement

The reflectivity of the cavity can be deduced by measuring either ring-down time or the gases, the absorption coefficient of which is known. In this work the former way is adopted, bacause the latter way has an additional error source[73]. If the laser is switched off when the resonant signal exceeds the predetermined threshold, the transmitted intensity shows the decay signal which is termed as a ring-down signal. The temporal intensity is equated as

$$I_t(t) = I_t(0)\exp\left(-\frac{t}{t_{RD}}\right), \tag{3.5}$$

where t_{RD} is the ring-down time, which is expressed as

$$t_{RD} = \frac{L}{c(1-R)}. \tag{3.6}$$

To have a single exponential curve, the switching time has to be shorter than ring-down time which is in the order of micro second. The switching time of a mechanical chopper is limited to sub-millisecond and is not short enough. Usually the high speed switching is achieved by using an acousto-optic modulator (AOM). It is reported that a piezoelectric transducer (PZT) can be used to

generate a ring-down signal[74]. To apply this simple method, the cavity has to be stable. As noted above, in plasma wind tunnel measurements the cavity is under the mechanical vibration. Thus AOM is adopted in this work. For accurate measurement of ring-down signal, the high-resolution data acquisition systems is desired since the ring-down signal is an exponential decay and has a wide dynamic range.

3.2.6 Mirror mount

The location of cavity mirror is important in plasma wind tunnel measurements. In application of trace gas measurement, the mirrors are usually mounted as a window of a cell in which the measurement target is maintained. Highly sensitive measurement can be achieved with this configuration. In plasma wind tunnel measurement, the mirrors face to the plasma and dusty environment in the chamber. These environments contaminate the mirrors and degrade the sensitivity during the measurement. One way to avoid this contamination is to purge the mirrors with an inter gas. Another is to put the mirror outside the chamber. In the former way the purge gas might affects the arc discharge in the heater. Furthermore the alignment of the cavity is quite difficult after the evacuation. Thus the mirrors are mounted outside of chamber. The disadvantage of this method is that the chamber windows inside the cavity absorbed or deflected the laser and the resultant reflectivity gets lower than that of cavity without windows. Figure 3.5 shows the ring-down signals of two cases. The thickness of the windows is 2 mm and the reflectivity degraded by 0.002.

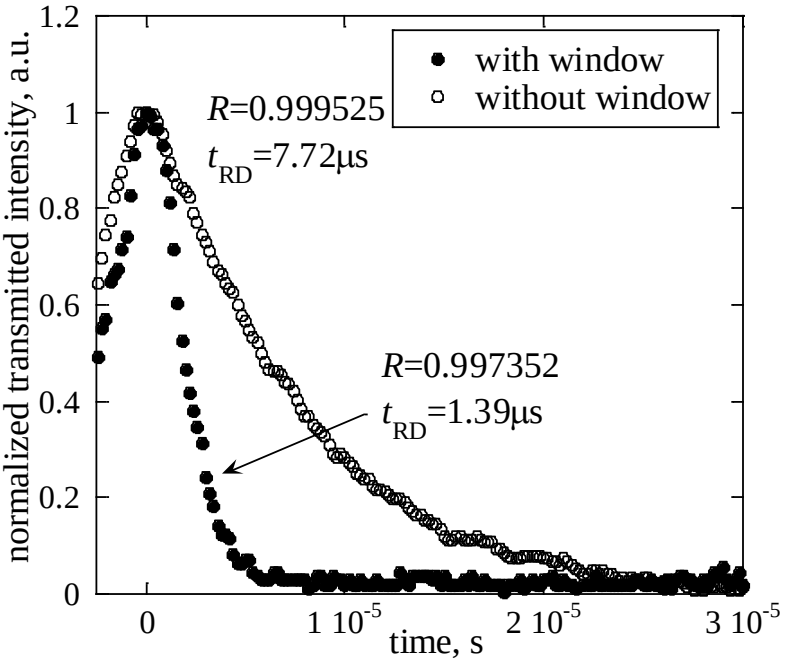

Figure 3.5 Ring-down signals of the cavity with and without windows.

3.2.7 Cavity enhanced absorption spectroscopy

When an absorber exists inside the cavity, the transmitted laser intensity is described as shown in Equation (3.7). In the region where absorbance is smaller than 0.01, the sensitivity is enhanced by 1/(1-*R*).

$$\frac{I_t}{I_0} = \frac{(1-R)^2 \exp(-kd)}{\{1-R\exp(-kd)\}^2} \tag{3.7}$$

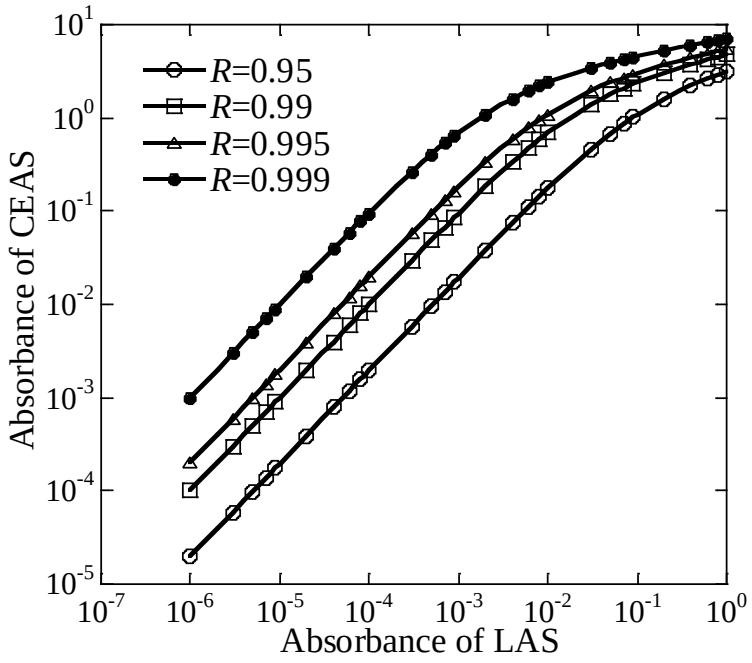

Figure 3.6 Sensitivity enhancement in CEAS.

3.2.8 Saturation effect in CEAS

When the lower state atoms are excited by an intense laser, number density of the lower state atoms depletes and the absorption is saturated. Saturation distorts the absorption profile and leads to the overestimation of Doppler broadening. In translational temperature measurement by LAS, the probe laser intensity has to be lower than one tenth of the saturation intensity[75]. In CEAS the transmitted laser intensity is quite low and usually it is detected by a photomultiplier tube. However the intra-cavity intensity is as high as the incident laser intensity. One needs to be careful about the probe laser intensity for accurate translational temperature measurement. Saturation in CEAS is different from that in LAS and the saturated profile broadening can't be corrected by the same manner as LAS. The schematic of absorbing atoms in CEAS is shown in Figure 3.7. The counter-propagating laser beams excite the lower state atoms. The atoms, which have no velocity component in the direction of beam propagation, absorb the laser as twice as other atoms absorbs. Thus saturation near the absorption center line is higher than other region.

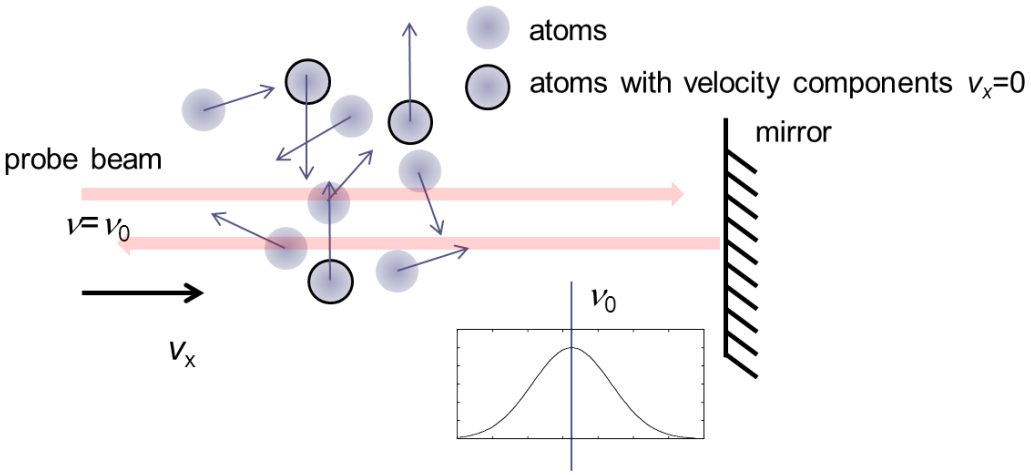

Figure 3.7 Schematic of atoms which absorb incident and reflected beams.

The resultant profile is calculated as shown in Figure 3.8. Saturated absorption shows a dip at the center. This is termed as Lamb dip[51]. The atoms in the sub-ground of Lamb dip are free from Doppler broadening. Thus the spectral width of Lamb dip is equal to the saturated homogeneous broadening. The Lamb dip shows the center frequency even in the overlapped two Doppler broadened profiles. This effect is intentionally utilized in saturated absorption spectroscopy (or Lamb dip spectroscopy, Doppler free spectroscopy) for accurate velocity measurement and frequency locking system to the absorption line. In addition, velocity-changing collision plays an important role. When the mean free time is longer than the interaction time with radiation field, velocity-changing collisions do not change the situation. However when the mean free time is much shorter than the interaction time with radiation field, the homogeneous broadening becomes wider.

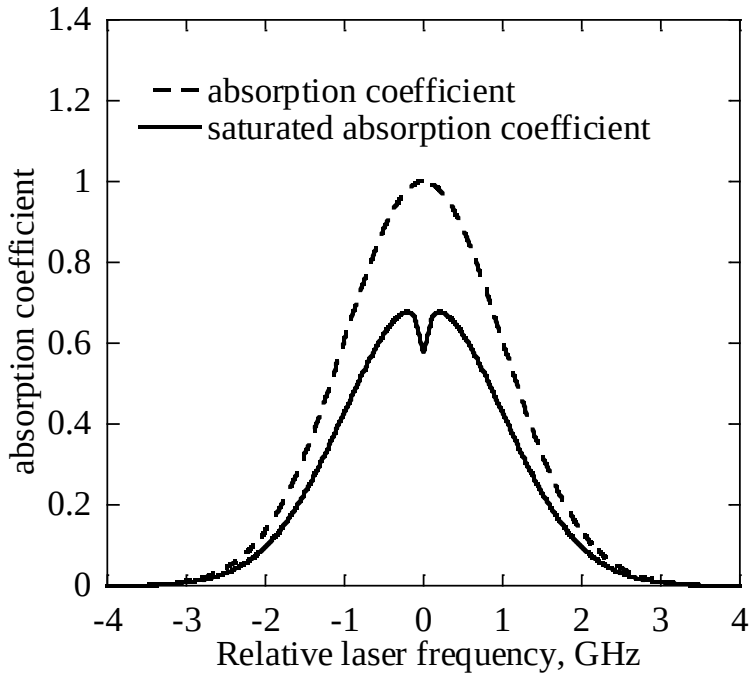

Figure 3.8 Lamb dip of saturated absorption signal.

3.3 Experimental Setup

3.3.1 Measurement system

The experimental setup is shown in Figure 3.9. The basic part of the setup was the same as that of single pass LAS. A tunable diode laser with external cavity (Velocity Model 6300; New Focus Inc.), whose linewidth was about 300 kHz was used as a light source. The laser wavelength was swept at the repetitive frequency of 1 Hz with the sweeping width of 36 GHz. The laser was operated around 777.19 nm which corresponds to the absorption line of atomic oxygen (3s ^{5}S-3s ^{5}P). The lower state of this transition was the metastable state. The relative laser frequency was monitored with an etalon whose free spectral range is 0.75 GHz. The microwave discharge plasma was generated on the optical table as a reference cell of atomic oxygen. Although argon plasma is easily generated by a glow discharge tube[76], it is difficult to generate atomic oxygen by the glow discharge tube. The reference cell enables to set the wavelength at the absorption line before the wind tunnel operation and to make it sure that the wavelength is around the absorption during the measurement even if the absorption signal is too small to be identified on an oscilloscope. At ring-down time measurement acousto-optic modulator (AOM, 1205C; Isomet Corp.) is used for the

switching of the laser. AOM consists of an optical crystal and PZT (piezoelectric transducer). When a longitudinal wave is generated inside a crystal ($PbMoO_4$) by PZT, it works as a grating and the laser is diffracted. The diffracted laser was used as a probe beam. The laser light was introduced to the wind tunnel through an optical fiber, and the output laser intensity was about 0.8 mW/mm^2. The intensity inside the cavity is estimated to be about 1 mW, which was not as high as to alter the plasma condition and influence temperature measurements. The optical cavity was built up by using the highly reflective mirrors (107586; Layertec GmbH) with a diameter of 1 inch. and a radius of curvature of 1500 mm. The cavity length was 1980 mm which corresponds to the free spectral range of 75.7 MHz. This value was small enough to resolve broadening of the absorption profile which was about 5 GHz. To avoid the contamination of the mirror caused by the wind tunnel flow, the mirror was mounted outside the chamber and the chamber windows between the mirrors were mounted at the Brewster angle. The polarization of the light was controlled by the polarization controller so as to be matched with the Brewster angle. The signals of etalon and photo detector at the microwave discharge tube were recorded by a logger (NR2000; KEYENCE Inc.) and the signal from the photo multiplier tube (PMT, H7732-10; Hamamatsu Photonics K.K.) was recorded by a digitizer (DP306; Agilent Technologies Inc.) on the PC-board. The effective area of PMT is 4×20 mm. To record all resonant signals in one sweep of the laser wavelength, the transmitted intensity was recorded for one sweep with a sampling rate of 2 MHz.

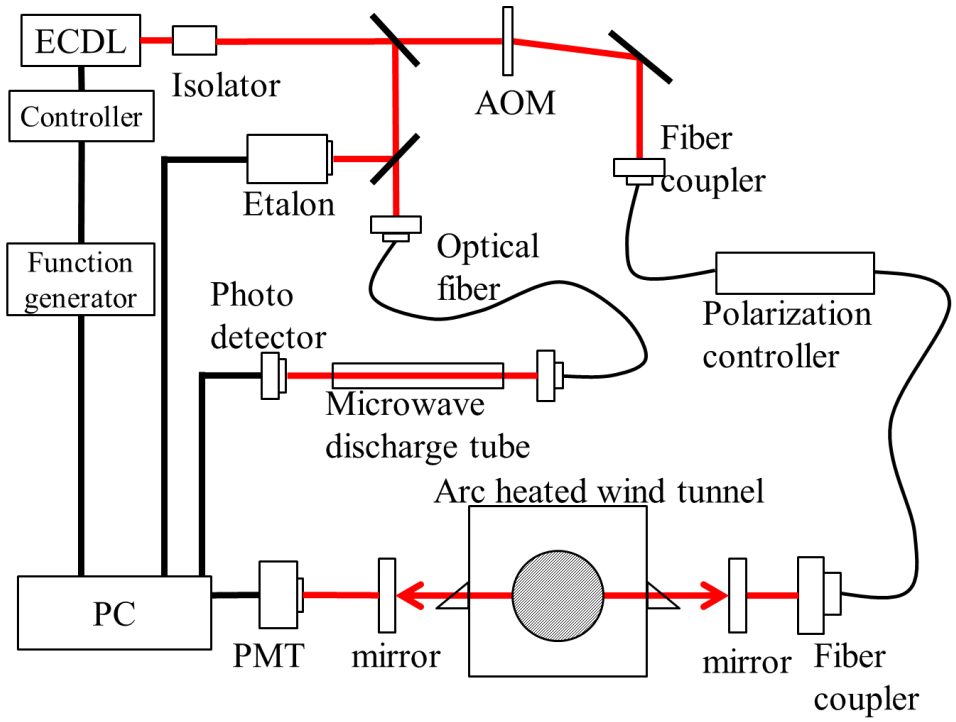

Figure 3.9 Schematic of optical setup of CEAS.

3.3.2 750 kW Arc-heated plasma wind tunnel

The operational conditions and photograph of the arc-heated wind tunnel flow in IAT-JAXA (Institute of Aerospace Technology, Japan Aerospace Exploration Agency) are shown in Table 3.1 and Figure 3.10. The specific enthalpy was measured by an energy balance method[77,78]. This wind tunnel consists of a constricted-arc heater, a conical nozzle with the throat diameter of 25 mm and nozzle exit diameter of 115 mm. Its nominal Mach number at nozzle exit is 4.8. The detail description on the 750 kW arc-heated plasma wind tunnel can be found on the report[79]. The absorption signal was not obtained in the free stream. The shock layer is generated over an ultra-high temperature ceramic (UHTC) of which diameter is 40 mm. The measured point is at 4 mm away from the UHTC's surface. The operation time is about 30 minutes. As mentioned above, in plasma wind tunnel measurements, mechanical vibration makes it difficult to achieve the purely longitudinal resonance condition. In the JAXA's 750kW arc-heated plasma wind tunnel, the vibration is induced mainly by high pressure cooling water system. The vibration of the chamber flange was measured by a laser displacement sensor, and it was found that the flange vibrates mainly with amplitude of 30 μm at 20 Hz.

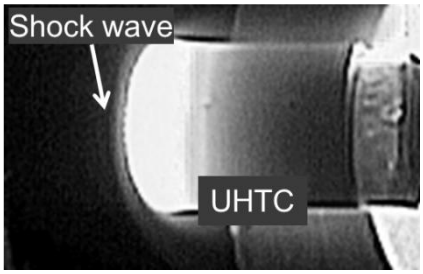

Figure 3.10 Photograph of UHTC (ultra-high temperature ceramics) with the shock wave in the arc-heated air plasma flow.

Table 3.1 Operational conditions of the 750 kW arc-heated plasma wind tunnel.

Parameter, unit	value
Current, A	700
Mass flow rate, g/s	10
Specific enthalpy, MJ/kg	21.8
Nozzle exit diameter, mm	115
Diameter of UHTC, mm	40

3.3.3 Estimation of refraction in the shock layer

The density difference between the free stream and shock layer might cause substantial refraction of laser as illustrated in Figure 3.11. Here the effect of refraction is roughly estimated. According to the Dale-Gladstone low, the refraction index, n is obtainable by

$$n = 1 + K_{\mathrm{G}}\rho \,. \tag{3.8}$$

K_{G} is the Dale-Gladstone constant. K_{G} of molecular nitrogen, atomic nitrogen and molecular oxygen are respectively 0.0002987, 0.000191 and 0.0002719 m^3/kg[1,2]. The free stream density can be estimated by

$$\rho_1 = \frac{p}{RT}\,, \tag{3.9}$$

assuming the ideal gas. The density behind the shock wave is calculated by using

$$\frac{\rho_2}{\rho_1} = \frac{(\gamma+1)M_1^2}{(\gamma-1)M_1^2+2}. \tag{3.10}$$

Now p, T, M_1 and γ are respectively assumed to be 120 Pa, 1000 K 4.8, and 7/5. n_1 and n_2 are estimated at 1.0000001 and 1.000006. Therefore, the displacement of the laser spot on the mirror is a few micro meters which is negligibly small. The laser diameter at the detector is 1.5 mm and the effective area of PMT is large enough to detect the slightly refracted laser.

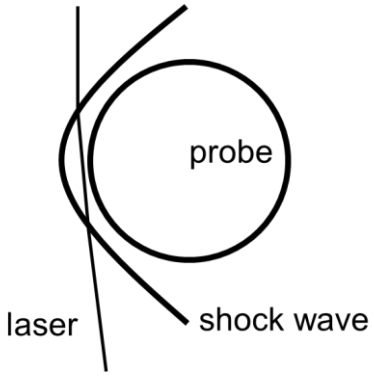

Figure 3.11 Schematic of refracted laser at the shock layer.

3.4 Results and Discussions

3.4.1 Reflectivity measurement

The ring-down signals under static and vibrating conditions are shown in Figure 3.12. By fitting the decay curve with Equation (3.5), the ring-down time and corresponding reflectivity were respectively deduced as 1.7106±0.0007 μs and 0.99611±0.0004 for static conditions, 1.0 μs and 0.9936±0.0004 for vibrating condition. The error was evaluated by the standard deviation of a hundred sweeps for static condition and thousand sweeps for vibrating condition. The decrease of reflectivity resulted from the fact that the high order resonant signals were induced by mechanical vibration and the number of reflection was reduced.

Table 3.2 Ring-down time and reflectivity of the cavity under non-vibrating and vibrating conditions.

	Ring-down time, μs	Reflectivity
Non-vibrating condition	1.7106±0.0007	0.9961±0.0004
Vibrating condition	1.0424±0.0004	0.9936±0.0004

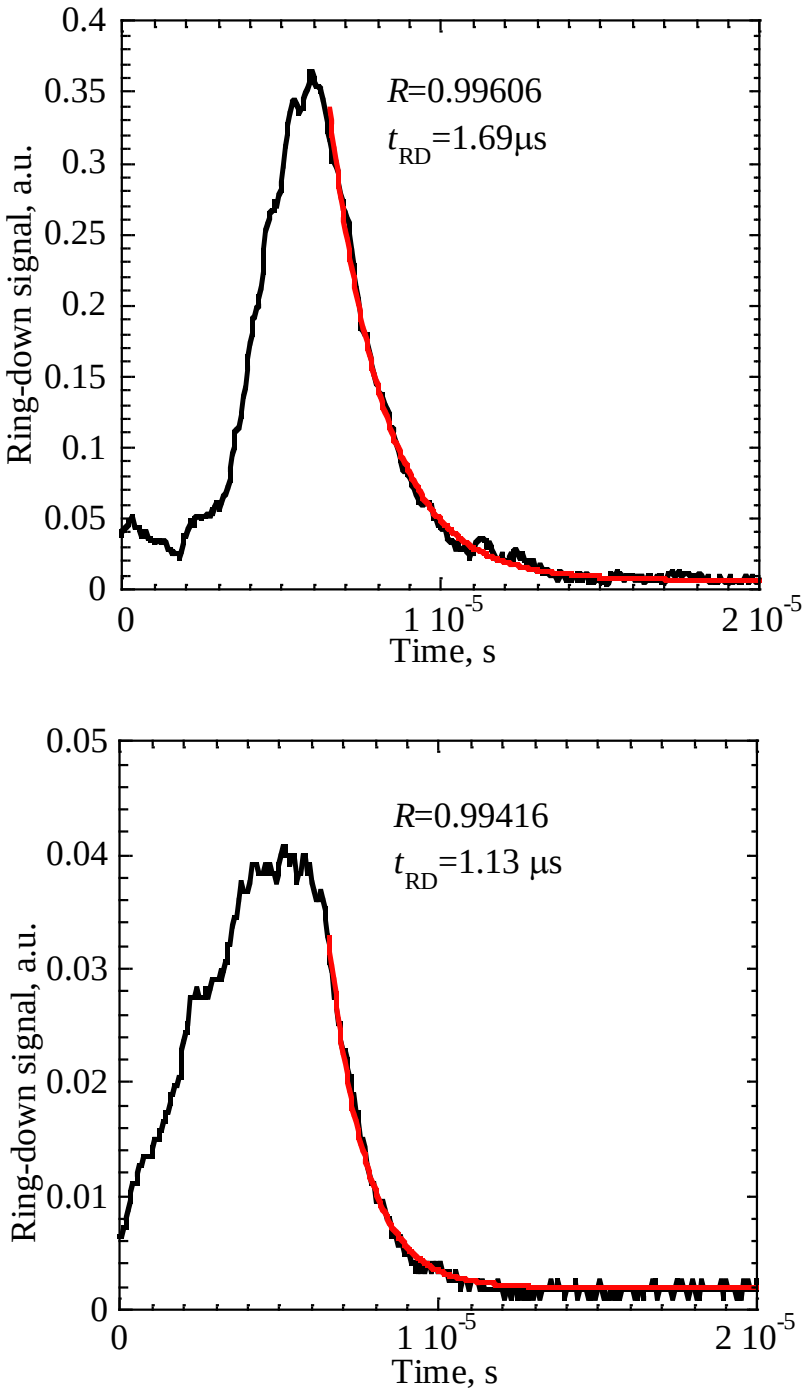

Figure 3.12 Ring-down signals under the non-vibrating (upper) and vibrating (lower) conditions.

3.4.2 Elimination of undesigned resonant signal from profile in one sweep

The transmitted intensity profile in one sweep and the absorption signal of the reference cell are shown in Figure 3.13. It is difficult to identify the absorption signal in one sweep, because the mechanical vibration induces resonant signals on the transverse mode as shown in Figure 3.14. In the data processing the resonant signals on the longitude mode was extracted as shown in Figure 3.15. The absorbance is also plotted in Figure 3.15. About 230 resonance signals were recorded in one sweep of laser wavelength. The absorption signal was not able to obtain in one sweep. The minimum detectable absorbance in one sweep was evaluated as 0.0015 from the standard deviation of absorbance.

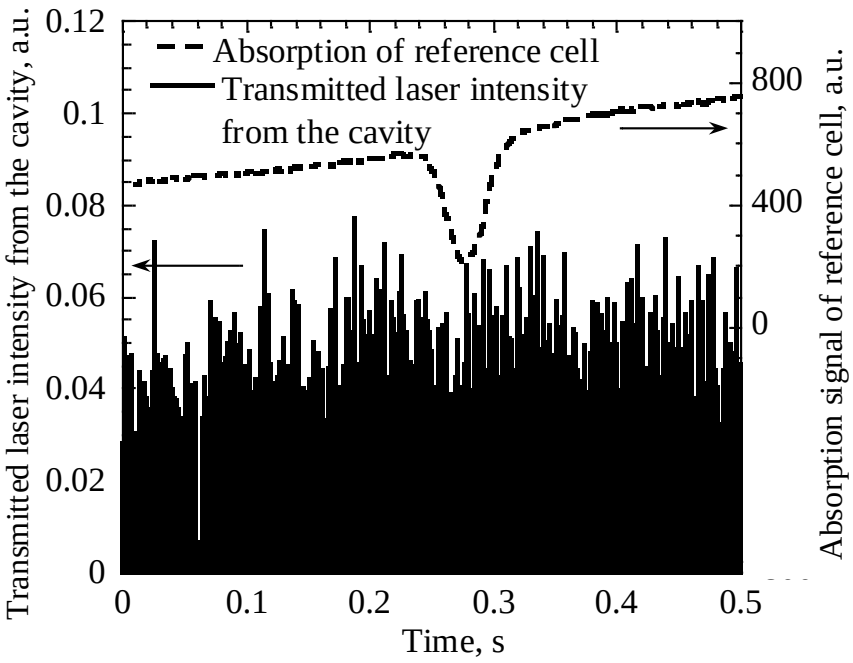

Figure 3.13 Transmitted laser intensity for one sweep of laser wavelength.

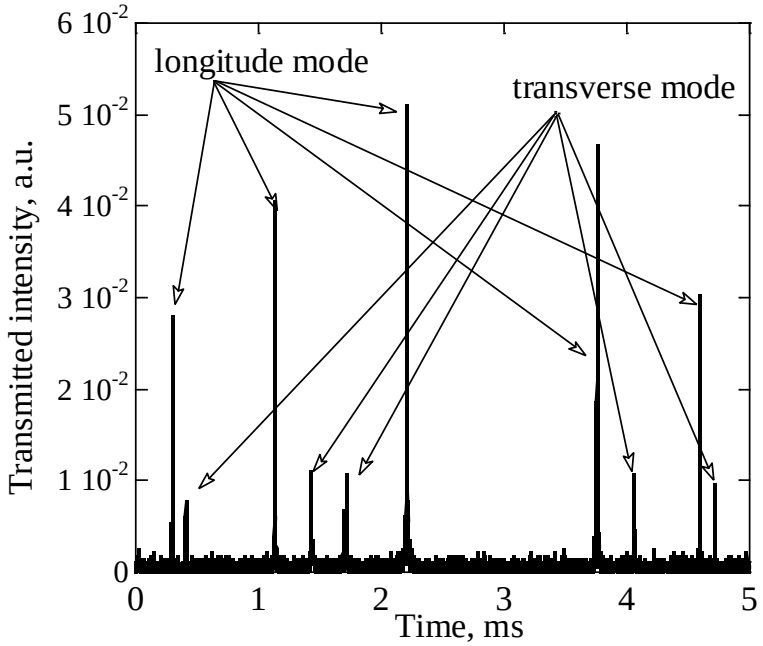

Figure 3.14 Resonance signal under mechanical vibration.

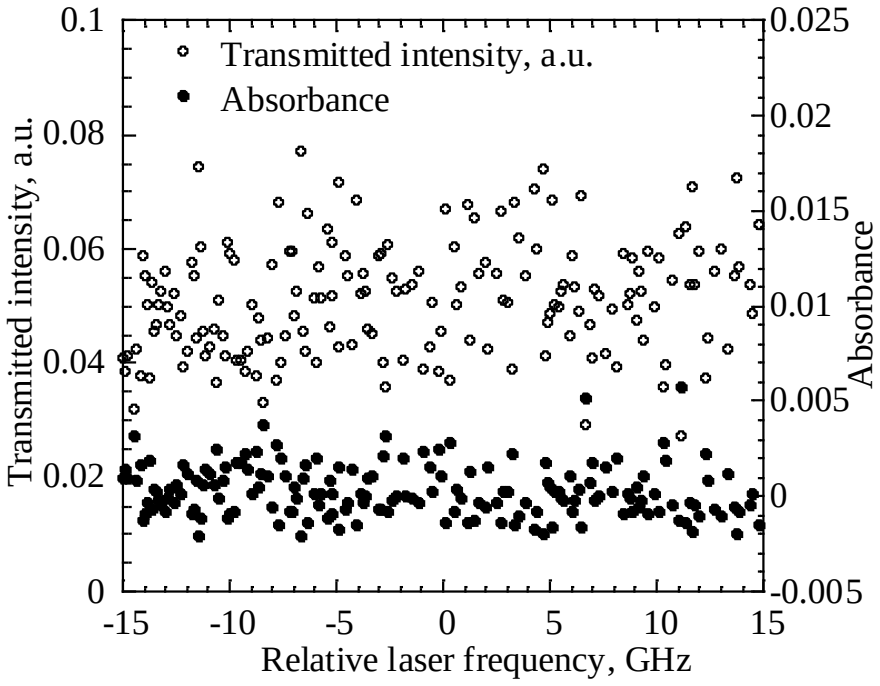

Figure 3.15 Peak intensity of longitudinal resonance signals in one sweep.

3.4.3 Averaging over a hundred sweeps of laser frequency

To get a smooth line of the absorption profile a hundred sweeps were recorded, and the peak value of the resonant signal was averaged over the frequency range of 37.5 MHz which corresponds to 5 % of the etalon's FRS. Averaging over 100 sweeps enabled identification of the absorption signal as shown in Figure 3.16. It took about 7 minutes to acquire all the data.

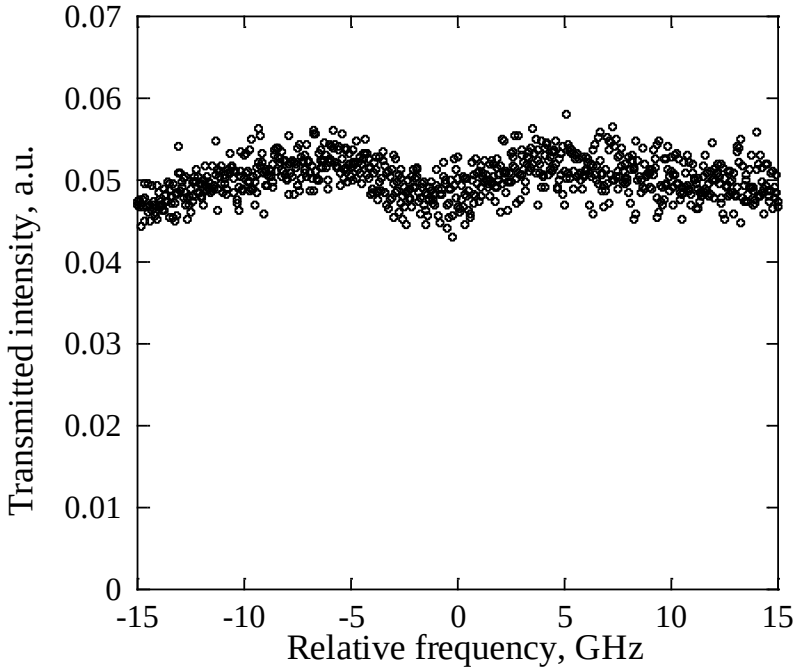

Figure 3.16 Transmitted peak intensity averaged over 100 sweeps.

Absorbance was calculated by Equation (3.7). The data were fitted by a Gaussian function with a least-squire method. The standard deviation of the residual was 3.0×10^{-4}. Thus it can be noted that the minimum detectable absorbance of this CEAS measurement was 3.0×10^{-4}. The typical value of minimum detectable absorbance of LAS is 0.01, and the sensitivity was enhanced by the order of two. FWHM of the profile was 4.5 GHz and corresponding translational temperature was 4200 K.

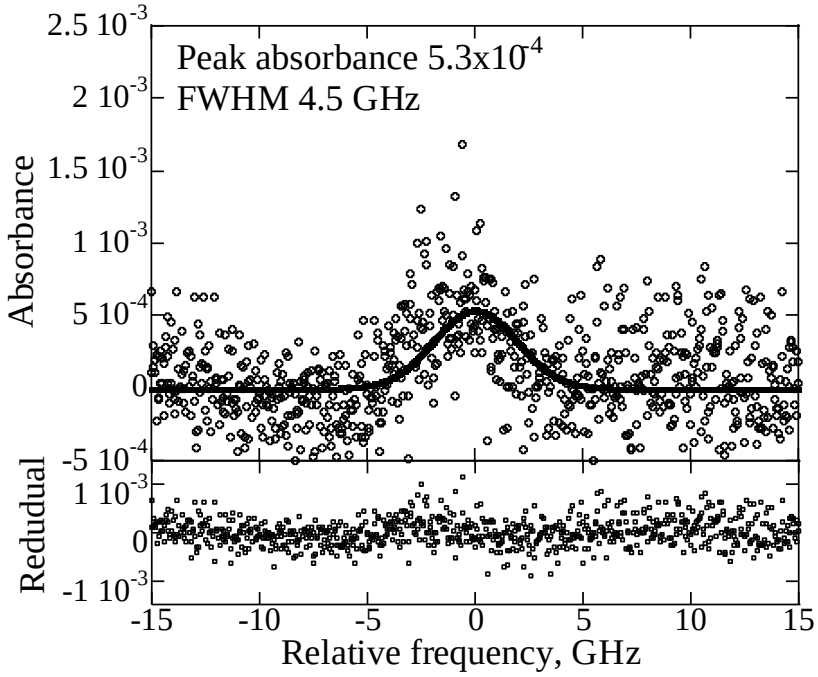

Figure 3.17 Absorption profile obtained by CEAS.

The measurement uncertainty in CESA was discussed by Takayanagi[80]. In this study absorbance of CEAS was 0.09 at the peak and the uncertainty of transmitted laser intensity was about 1%. Hence, the uncertainty of translational temperature was about 20 %. For the improvement of this uncertainty the more highly reflective cavity is required. The measured absorption signal was not spatially resolved because it is quite difficult to move the prove laser and optical cavity for Abel inversion with keeping the resonance condition. Although one possible way is to move the measurement target, usually the plasma generator is fixed at the chamber. Thus we need another method to achieve a spatially resolved and highly sensitive laser absorption spectroscopy. One candidate for this is the technique which is shown in Chapter 5. For the accurate estimation of enthalpy, there are some aspects to be investigated; flow velocity at the measurement point, thermal equilibrium, and thermal boundary layer thickness. With these uncertainties the specific enthalpy was roughly estimated to be 10 MJ/kg, assuming that the flow is stagnated and thermally equilibrium with 4200 K. Meanwhile, the specific enthalpy estimated by the energy balance method was 21.8 MJ/kg as shown in Table 3.1. The detailed measurements are required for the validation.

3.5 Summary

The absorption of atomic oxygen in the arc-heated air plasma flow was observed successfully by

CEAS. To our best knowledge, this is the first translational temperature measurement by laser absorption of atomic oxygen in the air plasma flow in the world. The undesired signals induced by the wind tunnel's mechanical vibration were eliminated in the data processing. The minimum detectable absorbance was 0.0015 and the sensitivity was improved by one order. A hundred sweeps were recorded and averaged. As a result the absorption was obtained successfully on the smooth base line. The peak absorbance and FWHM of absorption profile were respectively 5.3×10^{-4} and 4.2 GHz which corresponds to 4200 K. The minimum detectable absorbance was 3.0×10^{-4} and sensitivity was improved by the order of two.

Chapter 4 DIODE LASER-INDUCED FLUORESCENCE FOR AN OPTICALLY THICK PLASMA BY COMBINATION WITH LASER ABSORPTION SPECTROSCOPY

In optically thick plasma measurements, the absorption of laser and re-absorption (or self-absorption) of fluorescence distort a fluorescence profile and make it difficult to deduce Doppler broadening from the observed fluorescence broadening. Furthermore, when the probe laser intensity is high enough to induce saturation effect, saturation broadening makes the profile wider than the true profile. Correction methods for these effects are proposed and applied to the arc-heated argon plasma. The result shows a good agreement with the result of LAS which is spatially resolved with Abel inversion. This technique is valid only for measurement on the flow center axis, however the temperature on the center axis is the most important factor and this technique can be a power tool to obtain a 1-D distribution of temperature along the center axis.

4.1 Characteristics of Diode Laser-Induced Fluorescence

In ground state number density measurement, the energy gap between the ground state and an excited state is large and the corresponding absorption wavelength lies in the range of VUV. For this purpose, two photon absorption laser-induced fluorescence (TALIF) is usually adopted typically using a dye laser. Meanwhile, in translational temperature measurement, the transition does not need to be from the ground state. The importance lies in the line shape of the fluorescence profile and the fluorescence intensity calibration is not needed. The lower state atoms can be excited by one-photon absorption with a diode laser. When an external cavity diode laser is used, the line width is much narrower than that of dye lasers. This narrow band light source enables the accurate evaluation of the narrow profile. Diode Laser-induced fluorescence (DLIF) has been widely used in plasma diagnosis to measure temperature[81,82], and ion velocity distribution function[83]. Another difference between dye laser and diode laser is the required time period for one sweep of laser wavelength. In TALIF it takes tens of seconds to get one profile, while in DLIF the frequency of the diode laser can be sweep more rapidly. The investigation of DLIF spectroscopy is summarized in Table 4.1.

Table 4.1 Summary of DLIF measurement.

Author	Target	Excitation wavelength, nm	Fluorescence wavelength, nm	ref.
Galbács, G.	Li	670	670	[84]
Keesee, A.M.	Ar I, ArII, He I	750,442,501	667,668,668	[81,85]
Cleary, P.A.	NO_2	640	640	[86]
Severn, G	Ar II	664,669,689	461	[82,83,87]
Oksuz, K.	Ar II	668	442	[88]

4.2 Distortion of Fluorescence Profile

As described above, DLIF is a powerful tool for translational temperature measurements. In optically thick plasma measurements, however, the absorption of laser and re-absorption of fluorescence cause additional broadening of the fluorescence profile. Hertz corrected the fluorescence profile absorbed by flame[89]. In his correction method, 1-D fluorescence distribution along the laser was measured with an arrayed detector and the laser intensity along its pass was determined by iteration. Recently, the influence of optical thickness to the saturation curve was discussed by Vidal[90] with a closed two-level model. In these two works the non-symmetric 1-D distribution of the depleting laser was solved and the re-absorption of fluorescence was not taken into account. In plasma diagnosis, however, usually the axial symmetry of plasma can be assumed and the re-absorption needs to be considered. Therefore, in this paper a correction method for the absorption and re-absorption is proposed for axisymmetric plasma measurements. This is achieved in combination with LAS. This method does not need the iterative procedure and the both of absorption and re-absorption can be corrected in the same manner. The schematic of this method is shown in Figure 4.1.

Although an intense fluorescence can be achieved with an intense laser, it causes additional broadening of the profile. This broadening is termed as saturation broadening or power broadening. In translational temperature measurements the saturation regime is avoided and the linear region is used[91]. However in the application to small absorption coefficient measurement, the intense laser is preferable. Furthermore, in plasma diagnosis the saturation intensity is usually low because of its low pressure and the fluorescence profile tends to be saturated. In this case we need a correction method for saturation broadening.

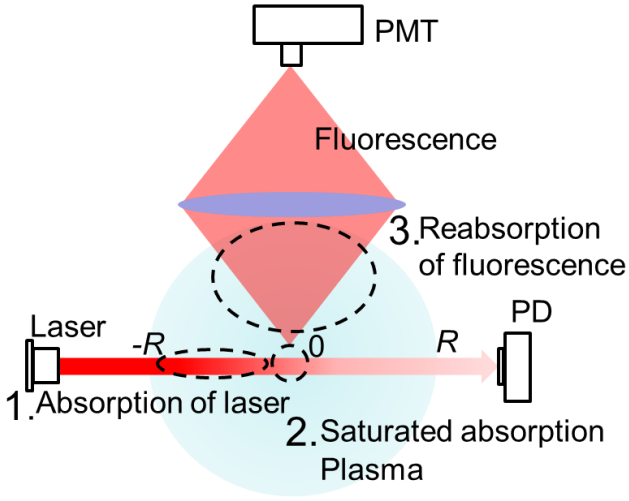

Figure 4.1 Schematic of LIF combined with LAS.

The correction methods for optical thickness and saturation broadening are demonstrated at an arc-heated argon plasma wind tunnel. The wavelength of excitation laser and fluorescence is 772.42 nm (Ar I, 4s ^{2}[1/2]°−4p ^{2}[1/2]). The measured point is on the axis of the axisymmetric flow. The result is compared with the result of LAS measurement for the validation.

4.3 Correction Methods

4.3.1 Absorption of laser

Taking the absorption of laser into consideration, the fluorescence is written as,

$$F_0 = Ck_s(0)I_0 \exp\left(-\int_{-R}^{0} k_s(x)dx\right) \tag{4.1}$$

where F_0, C, I_0, and k_s are the fluorescence intensity, experimental factor, incident laser intensity and saturated absorption coefficient, respectively. The coordinate system is shown in Figure 4.1. It should be noted that the absorption of laser is saturated because of its high irradiance. In the axisymmetric plasma absorbance from the incident edge to the center is a half of that from the incident edge to the edge;

$$\int_{-R}^{0} k_s(\nu, x)dx = \frac{1}{2}\int_{-R}^{R} k_s(\nu, x)dx \tag{4.2}$$

In accordance with Beer-Lambert law, integration in the right term is equated as

$$\int_{-R}^{R} k_s(\nu, x)dx = -\ln\left(\frac{I}{I_0}\right), \tag{4.3}$$

where I_0 and I are the incident and transmitted laser intensity, respectively. Thus absorption of laser can be corrected by monitoring the transmitted laser intensity.

4.3.2 Re-absorption of fluorescence

The fluorescence intensity is much lower than the saturation intensity, and the absorption of fluorescence is not saturated. Thus the correction for the re-absorption has to be done with the unsaturated absorption which is measured at low intensity. The fluorescence frequency is the same as the excitation frequency, and the measured fluorescence is expressed by

$$F = F_0 \exp\left(-\int_0^R k(x)dx\right) \tag{4.4}$$

where F and k are the measured fluorescence and unsaturated absorption coefficient, respectively. In the same manner as the correction for the absorption of laser, the absorption can be evaluated. This is valid when the distribution is axisymmetric.

$$\int_0^R k(x)dx = -\frac{1}{2}\ln\left(\frac{I}{I_0}\right) \tag{4.5}$$

4.3.3 Saturation broadening

The saturation effect in LIF has been investigated by some authors[92–94]. In their works Dye laser was often used for excitation and the laser spectral width was comparable to or wider than Doppler broadening. When the high intensity broadband laser is used, even at the spectral wing of laser, the laser intensity is high enough to induce substantial fluorescence as illustrated in Figure 4.2. The corresponding fluorescence profile shows wider broadening than the true profile. The broadening oriented by broadband laser is termed as a power broadening and theoretical and experimental approach has done. The effect of spatial distribution of laser intensity was also taken into considered and the modified saturation curve was proposed[95].

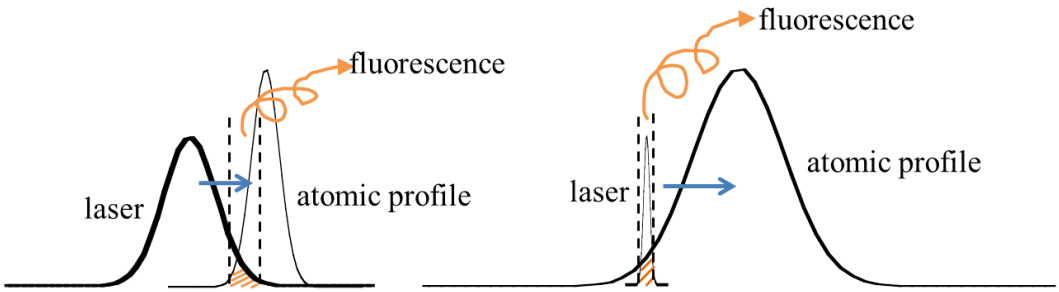

Figure 4.2 Schematic of spectral laser profile and atomic profile. (Left; broadband, right; narrowband).

In our condition, the absorption profile broadening is much wider than the laser spectral width. So the light source can be considered as monochromatic. In this case the broadening mechanism is different from that of power broadening and the same as that of LAS which is shown in Chapter 2. Saturation broadening can be corrected by performing saturated LAS. Saturated integrated absorption coefficient K_s is obtained using LAS by varying the laser intensity. By fitting K_s with Equation , K and I_S are obtainable. According to an earlier report[75], the true Doppler broadening is obtainable when the saturation parameter, S ($=I/I_s$) is less than 0.1. With a ratio of saturated broadening, $\Delta\nu_{Ds}$to the true Doppler broadening, $\Delta\nu_D$, the saturation effect is corrected. Correction factor for saturation broadening, α_s is expressed as

$$\alpha_s = \frac{\Delta\nu_{Ds}}{\Delta\nu_D} \tag{4.6}$$

Table 4.2 Summary of investigations on saturated LIF.

Author	Target	Remarks	Ref
Daily, J.W,1978	(Theoretical discussion)	To overcome the quenching effects	56
Daily, J.W,1978	(Theoretical discussion)	Saturation with a Gaussian beam	95
Takubo, 1983	CH in flame	Measurement of CH	93
Alkemade, 1985	Na in flame	Review on saturation curves	96
Goeckner, 1988	Ar II in plasma	Measurement in plasma	97
Goeckner, 1992	Ar II in plasma	Measurement in plasma	92
Levine, 2012	(Theoretical discussion)	Simple derivation of power broadening	98

4.4 Experimental Setup

4.4.1 Measurement system

Figure 4.3 shows the experimental setup. The basic component of the measurement system is the same as what is shown in Chapter 3. The laser wavelength was swept at the repetitive frequency of 0.5 Hz with the sweeping width of 20 GHz. To detect a small fluorescence signal, the excitation laser was modulated and phase sensitive detection was used with a lock-in-amplifier (SR830; Stanford Research Systems Inc.). The laser output was modulated with an acousto-optic modulator (1205C; Isomet Corp.) and introduced into the optical fiber. The modulation frequency was 20 kHz. The laser power at the output from the fiber was 1.0 mW and the laser spatial width at the measurement point was 0.4 mm. During the saturation measurement, the laser power was attenuated with neutral density filters. The fluorescence was collected with lenses and detected with a photo multiplier tube (H8249; Hamamatsu Photonics K.K). The time constant of lock-in-amplifier was 3 ms. The fluorescence, etalon, absorption signal were recorded with an oscilloscope (DSOX2004A, Agilent Technologies Inc.).

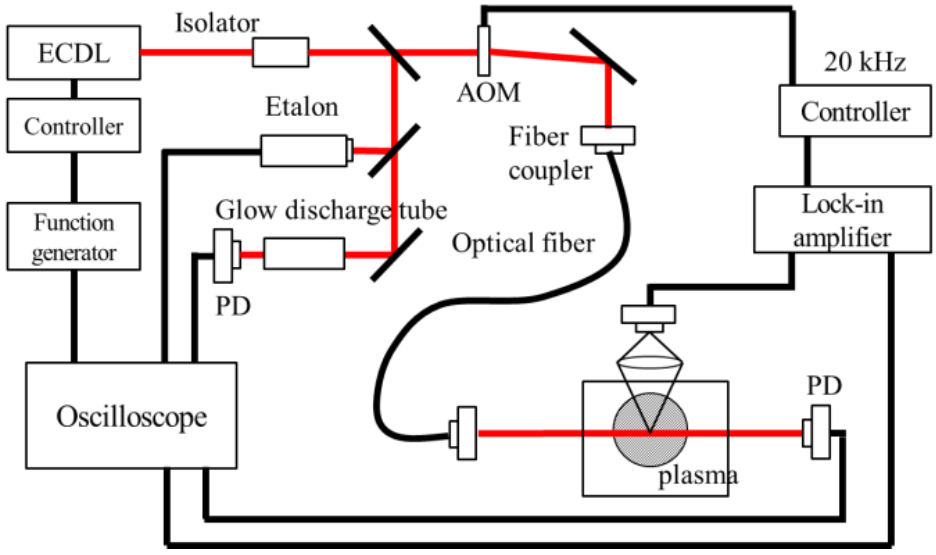

Figure 4.3 Schematic of experimental setup of LIF combined with LAS.

4.4.2 Arc-heated plasma wind tunnel

The argon plasma flow was generated with an arc-heated plasma generator and expanded with a nozzle. The cross sectional view of this generator is shown in Figure 4.4. The throat diameter was 2 mm and the nozzle exit was 30 mm. The tungsten cathode and cupper anode were used. The input power was 1.2 kW with a current of 50 A. The volume flow rate of argon was 4 slm and the chamber pressure was 20 Pa. The vacuum system consists of two series of rotary pump and mechanical booster pump. LIF and saturated LAS and LAS with Abel inversion were performed in the same operation. The total measurement time is around 20 minutes.

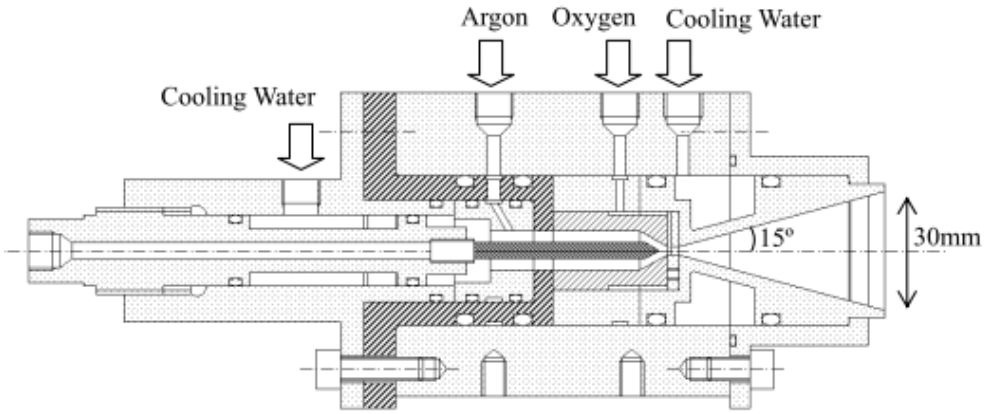

Figure 4.4 Schematic of arc-heated plasma wind tunnel.

Table 4.3 Operational condition of arc-heated plasma wind tunnel.

Parameter, unit	value
Input power, kW	1
Volume flow rate of Ar, slm	4
Plenum pressure, kPa	50
Chamber pressure, Pa	20

4.5 Results and Discussions

The saturated LAS was performed with varying laser intensity from 1 μW to 0.97 mW. Figure 4.5 shows saturated integrated absorption coefficient with the fitting curve and FWHM of saturated profile. The saturation intensity was estimated at 86 μW. The unsaturated absorbance was 0.403 at the peak and the unsaturated broadening was 1.80 GHz. The most saturated absorption profile was obtained at the laser power of 0.97 mW. At this power the saturation the saturated absorbance was 0.11 at the peak and saturated broadening was 1.94 GHz. Thus the ratio of saturated broadening to the true broadening was 1.08. The uncertainty of this ratio was estimated at 5% from Equation (4.6) and (4.6).

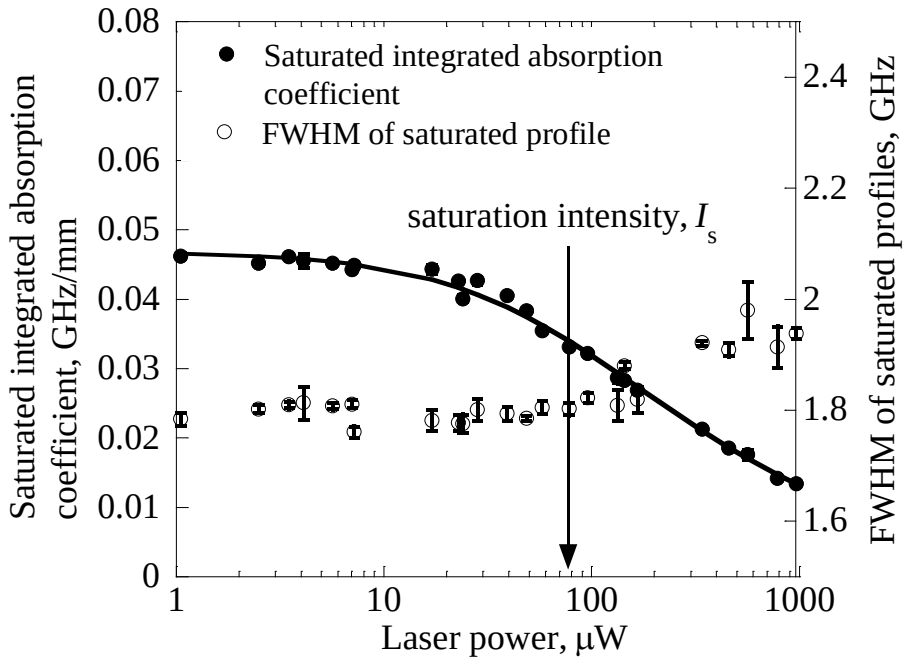

Figure 4.5 Saturated integrated absorption coefficient and as a function of laser power.

The LIF profile was obtained with the maximum laser power, 0.97 mW. The observed fluorescence broadening was 2.20 GHz. The uncertainty of fluorescence broadening can be evaluated by the uncertainty of fluorescence intensity as shown in Equations (4.6) and (4.1) and in this measurement its uncertainty was about 5%. The broadening effect by optical thickness was corrected by using Equation (4.3) and (4.5). Figure 4.6 shows the measured fluorescence profile and the corrected profiles. The broadening corrected for optical thick ness was deduced as 2.11 GHz. The

uncertainty in the correction for optical thickness is related to the uncertainty of laser intensity measurement as shown in Equations (4.1)-(4.5), and its uncertainty was less than 1%. As mentioned above, the ratio of saturated broadening to the true broadening was 1.08. Thus true Doppler broadening was 1.96 GHz and corresponding translational temperature was 1990 K. The total uncertainty in these correction methods for temperature measurement was estimated at about 10%. The broadening of observed profile and corrected profiles are tabulated in Table 4.4. Since LIF was performed at the saturation region (I/I_s=11) the influence of the absorption of laser was minor.

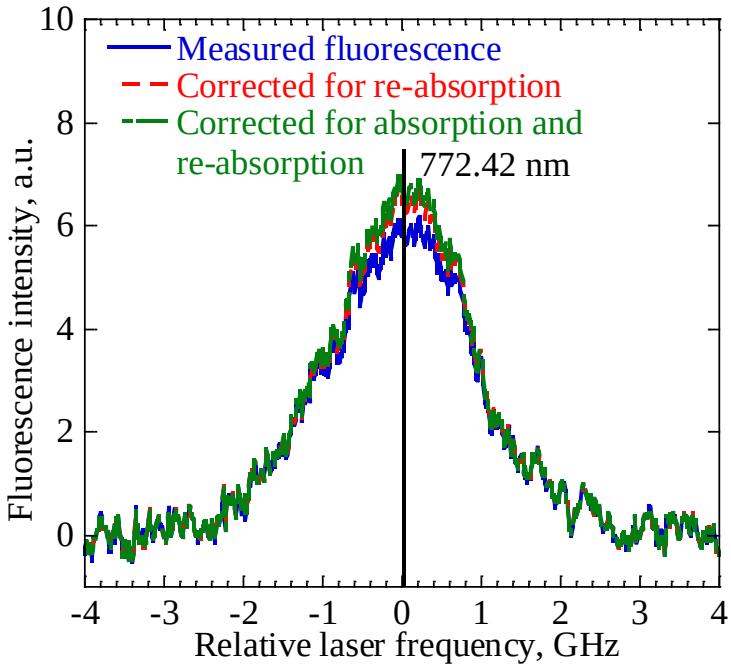

Figure 4.6 Measured and corrected fluorescence profiles of argon.

Table 4.4 Full width at half maximum (FWHM) and temperature of distorted profiles.

	FWHM, GHz	Temperature, K	Ratio of estimated temperature to true temperature
Profile distorted by re-absorption	2.04	2150	1.08
Profile distorted by absorption	1.98	2030	1.02
Profile distorted by saturation	2.11	2310	1.16
Observed profile	2.20	2510	1.26
True profile	1.96	1990	1

For the validation of this correction method the temperature distribution was obtained by LAS with Abel inversion as shown in Figure 4.7. Absorbance was obtained with spatially sweeping the probe laser by 1 mm. For the fitting of absorbance as a function of probe-laser position, the following function is used.

$$\left(a_1 y^4 + a_2 y^2 + 1\right)\exp\left(-\alpha y^2\right) \tag{4.7}$$

a_1, a_2, α are fitting parameters. The laser power was attenuated to 2.5 μW to avoid the saturation. At the center the temperature was estimated at 2050±100 K. The present result of DLIF shows good agreement with the result obtained by LAS which is spatially resolved by Abel inversion as shown in Table 4.5.

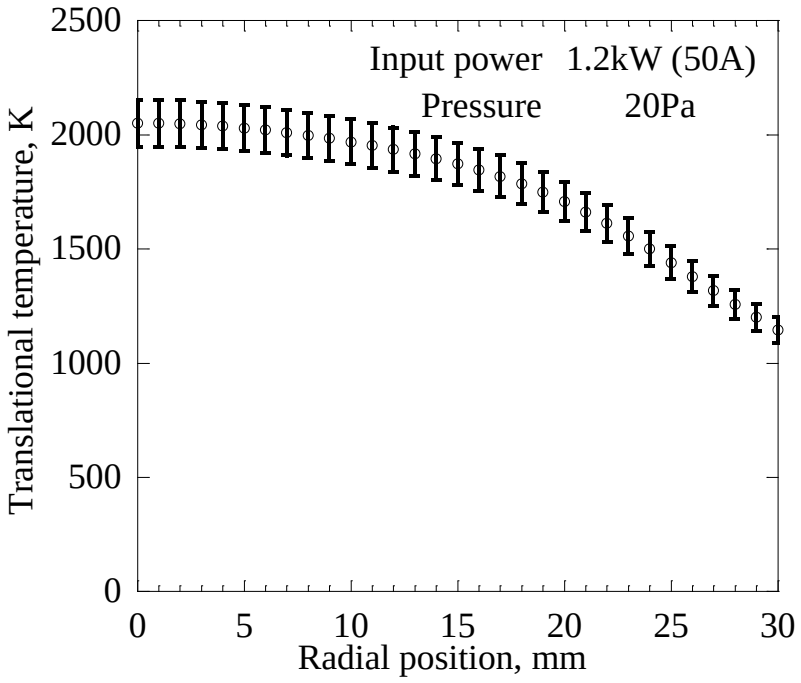

Figure 4.7 Temperature distribution obtained by laser absorption spectroscopy with Abel inversion.

Table 4.5 Temperature obtained with DLIF and LAS.

DLIF combined with LAS	LAS with Abel inversion
1990±200 K	2050±100 K

Figure 4.8 shows the ratio of estimated temperature to true temperature as a function of saturation parameter, S ($=I/I_S$). The contribution of three effects to the distortion is indicated. The peak absorbance is 0.4. The re-absorption of fluorescence is not saturated and independent of the laser intensity. As the laser intensity increases the absorption of laser is saturated and the distortion effect gets minor. When the saturation parameter is higher than 50, the error oriented by the absorption is less than 1 %. In the region where S is higher than unity saturation broadening is the most dominant in the distortion effects. Even if DLIF is performed with a low power laser and saturation is avoided, temperature is overestimated by about 10 %. Thus the correction is necessary to obtain the accurate temperature.

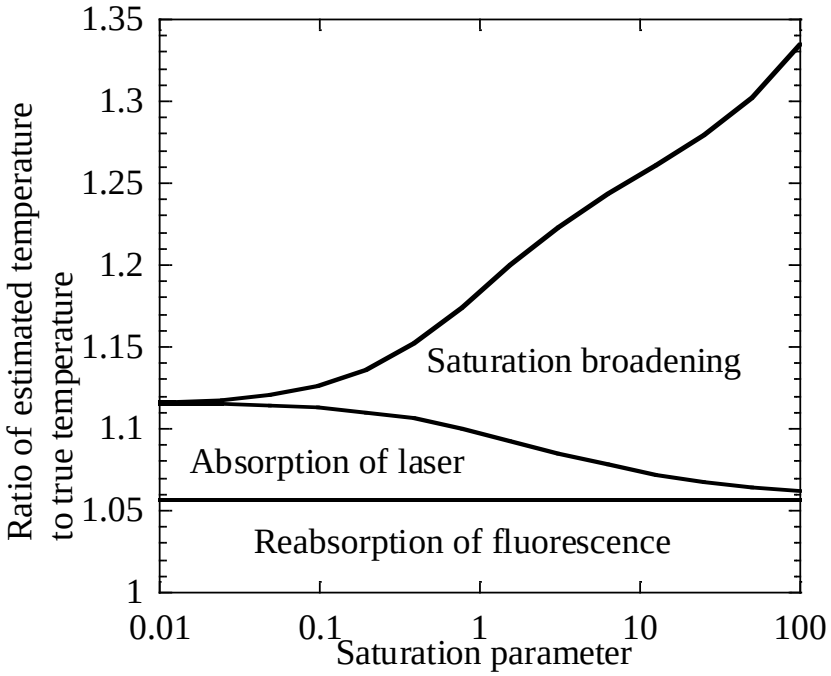

Figure 4.8 Ratio of LIF temperature (without correction) to true temperature as a function of saturation parameter, I/I_s. Absorbance is 0.4.

4.6 Summary

The distorted LIF profile was corrected using LAS data. For laser absorption and fluorescence re-absorption correction, saturated and unsaturated line-of-sight absorbance was measured by LAS. Saturation broadening was corrected with the ratio of saturated broadening to the unsaturated broadening in LAS. The Doppler broadening was corrected as 1.96 GHz, and the translational

temperature was 1990±200 K. This value showed a good agreement with the result of spatially resolved LAS with Abel inversion. The contribution of three effects to distorted LIF profile was estimated theoretically as a function of saturation parameter S ($=I/I_s$), showing that in the region where S is higher than unity, saturation broadening is the most dominant. Although the present correction method is applicable only to the center measurement of axisymmetric plasma, this method is a powerful tool for temperature distribution measurements along the flow axis and extends the applicable region of LIF.

Chapter 5 DEVELOPMENT OF CROSS-BEAM SATURATED ABSORPTION SPECTROSCOPY FOR TRANSLATIONAL TEMPERATURE MEASUREMENT IN SHOCK LAYER

Currently there is no diode laser spectroscopic measurement to directly obtain translational temperature in a shock layer. As discussed in Chapter 1, it is difficult to apply LAS to an optically thick shock layer over a blunt body. Although DLIF combined with LAS enables correction of the distorted profile in optically thick plasma (see Chapter 4), the correction method can't be applied for the shock layer measurement. This is because the flow in the shock layer has a radial velocity and the absorption and re-absorption are respectively shifted to blue and red side. In this chapter, a novel technique which is termed as cross-beam saturated absorption spectroscopy is developed to measure translational temperature in the shock layer. Here, the plasma flow is in a transition region between the continuous flow and free molecular flow (Kn=0.1~1) with Mach number of 2.27. The shock wave is generated with a spherical probe whose diameter is 25.4 mm, and merged with a boundary layer. This technique can be applied to an absorber with an arbitrary distribution; not only to shock layer but also to a plume of the electric propulsion and CVD plasma.

5.1 History of Cross-beam Saturated Absorption Spectroscopy

Cross-beam saturated absorption spectroscopy (XBSAS) was developed by Goldsmith[99] in 1981 to obtain the number density distribution in a flame. This technique was developed as an extension of saturated absorption spectroscopy. In XBSAS the high power laser crosses with the probe beam and induce saturation only at the crossing point. The difference between saturated absorption and unsaturated absorption is the information only from the crossing point. In his work the relative value of number density was obtained rather than the absolute density as shown in Figure 5.1. After his demonstration, several works of XBSAS were continued in the field of flame measurement. The different kinds of two beams' configuration were proposed; single laser or two different lasers, and cw laser or pulsed laser. To improve the sensitivity the techniques of saturated interference spectroscopy and laser polarization spectroscopy are applied to the cross-beam spectroscopy[100,101]. Not only the saturation effect but also the stark effect was also used in the cross-beam spectroscopy[102,103]. Since the last publication of Zizak[104], however, the related measurement has not been reported. In their works the advantage over LIF was focused. To avoid the collisional

quenching effect, they utilized XBSAS. In fact, XBSAS also has the drawback of difficulty in the optical alignment and insensitivity of measurement. In number density measurement in flame, TALIF was preferred and has remained popular and XBSAS is not used nowadays. The cross-beam spectroscopic measurements are summarized in Table 5.1.

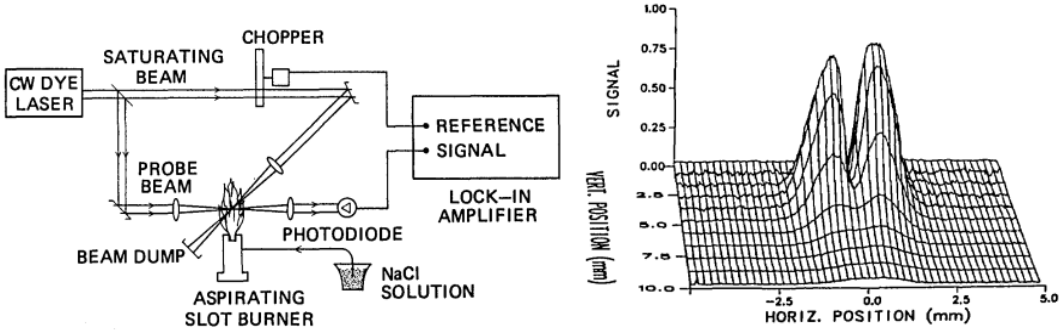

Figure 5.1 Schematic of the experimental setup of XBSAS and the relative number density distribution[99].

Table 5.1 Summary of cross-beam spectroscopy

Auther, Year	Target	Species	Probe beam	Second beam	Reference
Goldsmith, 1981	burner, 1 atm	Na,589 nm	CW Dye	same as probe	[99]
Kychakoff,1984	flame,1 atm	OH,	Ring Dye	Pulsed Dye	[105]
Walters,1984	flame	Sr	Pulsed Dye	same as probe	[106]
Walters,1984	ICP	Sr, 460 nm Ba^+, 455 nm	Pulsed Dye	same as probe	[107]
Zizak, 1987	flame	OH	Pulsed Dye	same as probe	[104]

Although XBSAS is not often used in number density measurement in flame, in low pressure plasma measurement XBSAS can be a powerful tool to measure translational temperature. In the previous work, saturation was induced by a high power and broadband dye laser. Goldsmith mentioned that the gain in spatial resolution was accompanied by a loss of spectral resolution[99]. In low pressure plasma, the saturation intensity is much lower than that in atmospheric pressure, because the saturation intensity is proportional to the homogeneous broadening (see Chapter 2). Therefore one does not need a powerful dye laser to induce the saturation effect. Instead, narrow band external cavity diode laser can be used as a saturating beam. The narrow band light source enables to evaluate the Doppler broadened profile and translational temperature measurement is possible.

5.2 Advantage over LIF

LIF and XBSAS are similar spectroscopic methods. In both measurements, point measurement is possible and the high intensity laser improves the signal to noise ratio of measurement. XBSAS, however, has some advantages over LIF with regard to translational temperature measurement. In LIF, high intensity laser distorts the profile because of saturation. Additional correction method which is shown in Chapter 4 is required. In contrast, measured broadening of XBSAS profile converges to true broadening as the saturating beam intensity increases (see 5.3.3). Another advantage is that the simplicity of the detection system. In LIF one needs to collect fluorescence with lenses. In XBSAS the probe laser is detected by a photo detector. The collecting lenses are not required and the detector can be put away from the measurement target.

5.3 Principle of Cross-beam Saturated Absorption Spectroscopy

5.3.1 Deviation of absorption coefficient at the crossing point

Figure 5.2 shows the schematic of XBSAS. A probe beam with low intensity crosses with a saturating beam which has high intensity. In this thesis, the same light source is used for the probe beam and saturating beam and the both beams have an identical wavelength. Here the axisymmetric distribution is considered for simplicity; however the following derivation is valid also for arbitrary distribution. Without the saturating beam absorbance is the integration of absorption coefficient from -R to R along the laser pass as follows.

$$-\ln\left(\frac{I_{\mathrm{p}}}{I_{\mathrm{p0}}}\right)=\int_{-R}^{R}k(x)dx \quad . \tag{5.1}$$

I_{p} and I_{p0} are respectively the transmitted and incident probe beam intensity. When the saturating beam crosses with the probe beam at x=x_0 with a small width of Δx, the partly saturated absorbance is described as

$$-\ln\left(\frac{I_{\mathrm{ps}}}{I_{\mathrm{p0}}}\right)=\int_{-R}^{x_0-\Delta x/2}k dx+\int_{x_0-\Delta x/2}^{x_0+\Delta x/2}k_{\mathrm{cs}}dx+\int_{x_0+\Delta x/2}^{R}k dx \quad . \tag{5.2}$$

I_{ps} is the transmitted probe beam intensity which crosses with the saturating beam. k_{cs} is the cross-beam saturated absorption coefficient. Subtracting Equation (5.2) from Equation (5.1), the information at the crossing point can be extracted as follows.

$$-\ln\left(\frac{I_{\mathrm{p}}}{I_{\mathrm{ps}}}\right)=\left\{k\left(x_0\right)-k_{\mathrm{cs}}\left(x_0\right)\right\}\Delta x \tag{5.3}$$

Here, $k(x)$ is assumed to be uniform in the crossing area. The fluorescence induced by the saturating beam can be neglected because its intensity is much smaller than the probe beam intensity.

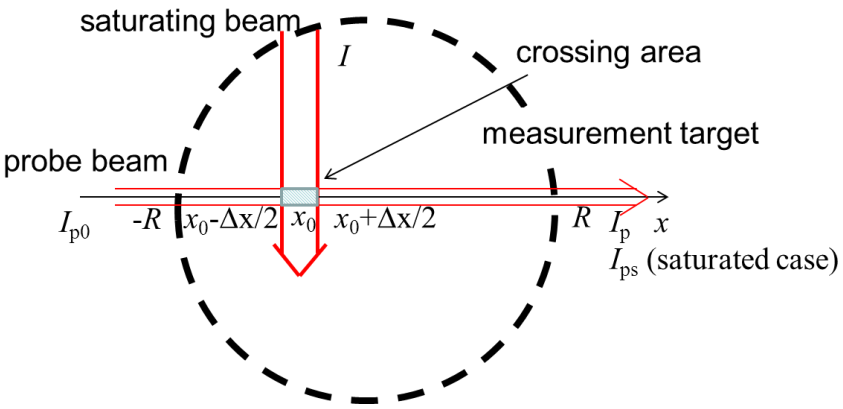

Figure 5.2 Schematic of cross-beam saturated absorption spectroscopy.

In most cases, difference between I_{p} and I_{ps} is so small that it is difficult to deduce $k(x_0)$-$k_{\mathrm{s}}(x_0)$ from $-\ln(I_{\mathrm{p}}/I_{\mathrm{ps}})$ by measuring I_{p} and I_{ps} independently. Thus a phase sensitive detection system was implemented. When the saturating beam intensity is modulated with a switching system, the probe laser intensity shows the oscillating signal as shown in Figure 5.3. In fact, the oscillating signal is not distinguishable from the noise. By using a lock-in-amplifier, only the oscillation which has the modulation frequency can be extracted. The output of the lock-in-amplifier is the oscillation's effective amplitude. Thus it is useful to express Equation (5.3) with ΔI ($=I_{\mathrm{p}}$-I_{ps}). When x is much smaller than unity, $\ln(1-x)$ can be approximated by x. Thus Equation (5.3) can be rewritten as

$$-\frac{\Delta I}{I_{\mathrm{ps}}}=\left\{k\left(x_0\right)-k_{\mathrm{cs}}\left(x_0\right)\right\}\Delta x \tag{5.4}$$

.

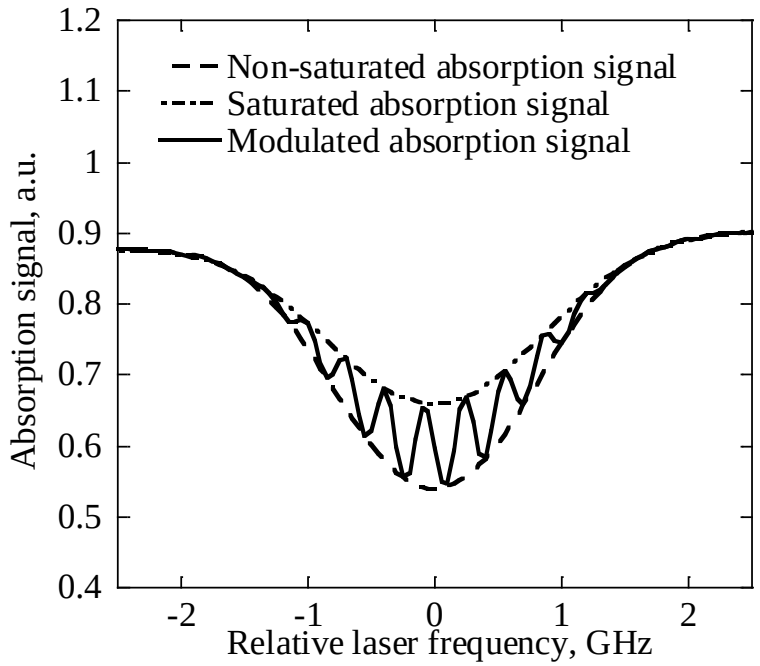

Figure 5.3 Schematic of saturated and unsaturated absorption signals.

5.3.2 Line shape of profile in XBSAS

The line shape of XBSAS signal shows narrower width than the LAS profile. For translational temperature measurements, the spectral line shape function of Equation (5.4) has to be evaluated as a function of temperature. Equation (5.4) is rewritten as

$$-\frac{\Delta I(\nu)}{I_{ps}(\nu)} = \{k(\nu) - k_{cs}(\nu)\}\Delta x \tag{5.5}$$

Figure 5.4 shows the atoms with an arrow of thermal motion direction. The probe beam and saturating beam respectively propagate in the direction of x and y axis with the same frequency. As explained in Chapter 2 when the laser with a frequency of $\nu_0+\Delta\nu$ transmits the plasma, only the atoms with a velocity component of $(\Delta\nu/\nu_0)c$ in the direction of laser propagation, absorbs the laser. In the single laser absorption spectroscopy, the absorption represents the velocity distribution function along the laser pass and in thermal equilibrium state, a Maxwellian velocity distribution yields the line-shape of the Gaussian function. Meanwhile, in the cross-beam laser absorption spectroscopy, the atom which absorbs the both of probe and saturating beam, must have the same velocity component in the direction of x and y axis. Hence the number of absorbing atoms is lower than that of single beam LAS. From Equation (2.6), the number density of atoms which absorb the

both beams with a frequency of from ν to ν+dν is deduced as following.

$$n_i(\nu)d\nu = N_i\left[\frac{c}{\nu_0\nu_p\sqrt{\pi}}\exp\left\{-\left(\frac{c(\nu-\nu_0)}{\nu_0\nu_p}\right)^2\right\}\right]^2 d\nu \tag{5.6}$$

Absorption coefficient can be divided into two groups as Equation (5.7). One is the group in which atoms have the same velocity components for *x* and *y* direction, and in the other group the velocity differs for *x* and *y* direction.

$$\begin{aligned} k(\nu) &= K_i \times \frac{\sqrt{2\ln 2}}{\pi^{3/2}}\frac{\Delta\nu_L}{\Delta\nu_D}\int_{-\infty}^{\infty}\frac{\exp\left\{-(\nu_\xi-\nu_0)^2/(\Delta\nu_D/2\sqrt{\ln 2})^2\right\}\times\alpha d\nu_\xi}{(\nu-\nu_\xi)^2+(\Delta\nu_L/2)^2} \\ &+ K_i \times \frac{\sqrt{2\ln 2}}{\pi^{3/2}}\frac{\Delta\nu_L}{\Delta\nu_D}\int_{-\infty}^{\infty}\frac{\exp\left\{-(\nu_\xi-\nu_0)^2/(\Delta\nu_D/2\sqrt{\ln 2})^2\right\}\times\{1-\alpha\}d\nu_\xi}{(\nu-\nu_\xi)^2+(\Delta\nu_L/2)^2} \\ \alpha &= \exp\left\{-(\nu_\xi-\nu_0)^2/(\Delta\nu_D/2\sqrt{\ln 2})^2\right\} \end{aligned} \tag{5.7}$$

In cross-beam saturated absorption coefficient only the first term is saturated. The absorption coefficient difference between non-saturated case and cross-beam saturated case is expressed as

$$\begin{aligned} k(\nu)-k_{cs}(\nu) = K_i\frac{\sqrt{2\ln 2}}{\pi^{3/2}}\frac{\Delta\nu_L}{\Delta\nu_D}\{&\int_{-\infty}^{\infty}\frac{\exp\left\{-2(\nu_\xi-\nu_0)^2/(\Delta\nu_D/2\sqrt{\ln 2})^2\right\}d\nu_\xi}{(\nu-\nu_\xi)^2+(\Delta\nu_L/2)^2} \\ &-\int_{-\infty}^{\infty}\frac{\exp\left\{-2(\nu_\xi-\nu_0)^2/(\Delta\nu_D/2\sqrt{\ln 2})^2\right\}d\nu_\xi}{(\nu-\nu_\xi)^2+(\Delta\nu_L\sqrt{1+I/I_s(\nu)}/2)^2}\} \end{aligned} \tag{5.8}$$

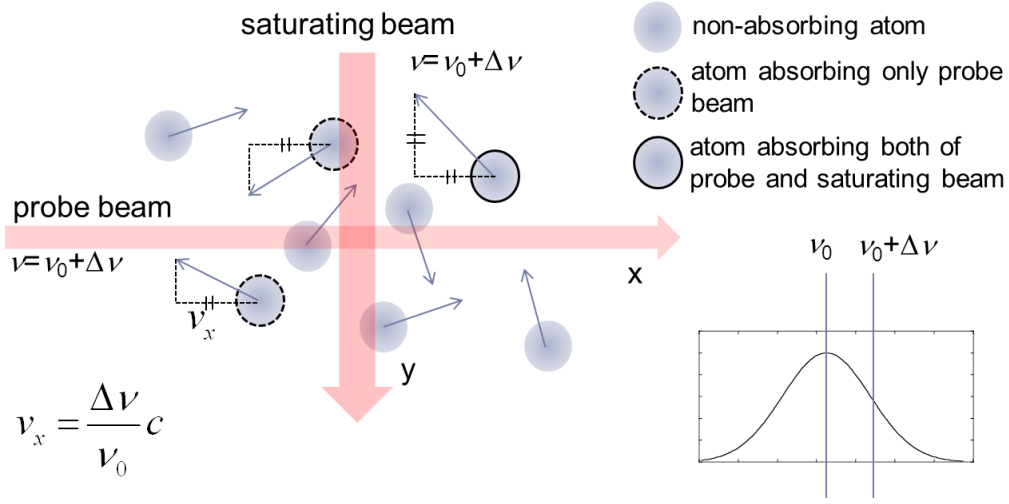

Figure 5.4 Schematic of atoms which absorbs the probe beam and saturating beam.

The saturation intensity should be modified from Equation (2.33). In XBSAS, the atoms which absorb the saturating and probe beams have a same velocity component in *x* and *y* directions. The frequency-selective $\bar{v}$ is

$$\bar{v}(\nu) = \sqrt{\frac{2(\nu-\nu_0)^2}{\nu_0^2}c^2 + \frac{k_B T_{tr}}{m}}. \tag{5.9}$$

The saturation intensity $I_s(\nu)$ is rewritten as

$$I_{cs}(\nu) = I_{cs}\sqrt{\frac{16\ln 2}{3}\frac{(\nu-\nu_0)^2}{\Delta\nu_D^2} + \frac{1}{3}}. \tag{5.10}$$

5.3.3 Dependency on saturating beam intensity

The measured profile varies with the saturating beam intensity. The XBSAS profiles simulated with Equation (5.8) are shown Figure 5.5 with different saturation parameters. Figure 5.6 shows a ratio of FWHM of XBSAS profile, $\Delta\nu_{D\_XBSAS}$ to true profile as a function of saturation parameter. In completely saturated region, Equation (5.8) can be written as

$$k(\nu) - k_{cs}(\nu) = K_i \frac{\sqrt{\ln 2}}{\pi^{3/2}} \frac{\Delta\nu_L}{\Delta\nu_D} \int_{-\infty}^{\infty} \frac{\exp\left(-2\left(2\sqrt{\ln 2}\nu/\Delta\nu_D\right)^2\right) d\nu_\xi}{(\nu-\nu_\xi)^2 + (\Delta\nu_L/2)^2}. \tag{5.11}$$

This function can be seen as a Voigt function whose Doppler broadening is $\Delta\nu_D/\sqrt{2}$. Therefore in Figure 5.6 the ratio converts to 0.7 (=$2^{-0.5}$).

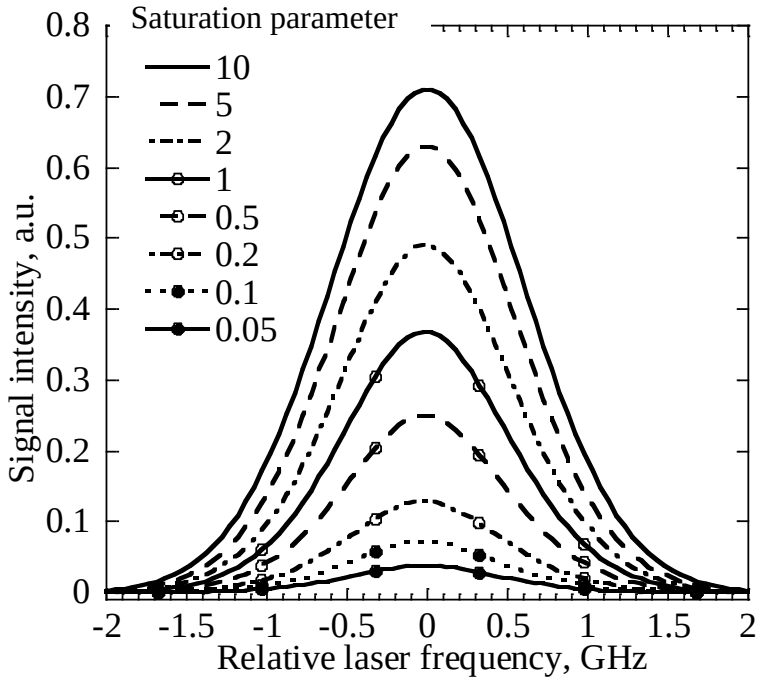

Figure 5.5 Simulated profile of XBSAS as a function of saturation parameter.

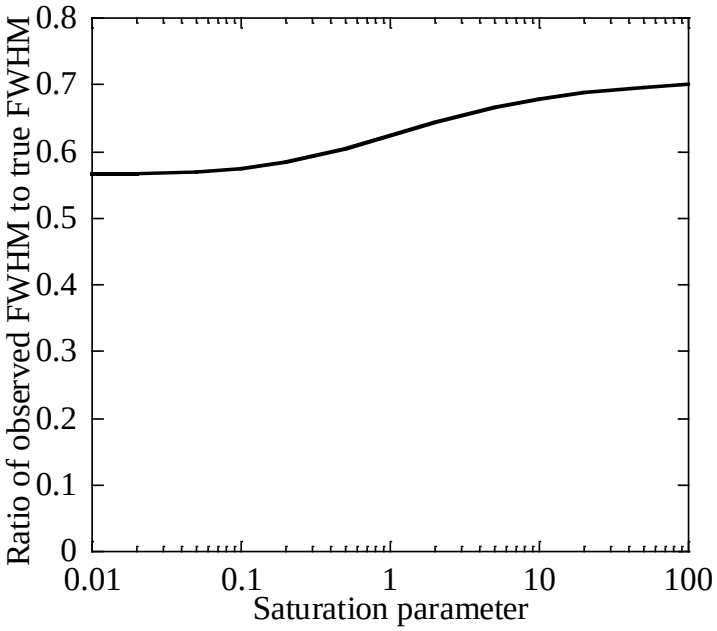

Figure 5.6 Ratio of FWHM of the XBSAS profile to true profile as a function of saturation parameter. (In plasma wind tunnel measurement Doppler broadening is much wider than other Lorentzian broadenings. In this thesis the profile is fitted by the Gaussian function.)

If the high intensity laser is used, measurement can be done at completely saturated region and broadening of the profile is not a function of saturating beam intensity. In this case one can obtain temperature easily.

$$T_{\mathrm{tr}} = \frac{mc^2}{4\ln 2 k {\nu_0}^2} \Delta \nu_{D\_\mathrm{XBSAS}}^2 \tag{5.12}$$

When degree of saturation is unknown, it has to be evaluated. There are two possible ways. One is to obtain the saturation curve as shown in Figure 5.6 by changing the saturating beam intensity in the wide range of saturation parameter, I/I_s. By fitting the saturated integrated absorption coefficient the saturation intensity can be estimated. The other is to conduct LAS with varying probe laser intensity. In this work the latter method was adopted. In the former method, it is possible to evaluate saturation at the crossing point. However in our measurement, the saturation parameter is limited in the range of from one to ten. The upper limit is determined by the maximum intensity of saturating beam. In such a limited range of saturation parameter, it is difficult to evaluate the saturation intensity accurately. Therefore saturated absorption was evaluated by changing the probe laser intensity. Once the saturation intensity is obtained, a ratio of $\Delta\nu_{D\_\mathrm{XBSAS}}$ to $\Delta\nu_{D,}$ α is known by using the curve in Figure 5.6. Finally, translational temperature can be obtained as

$$T_{\mathrm{tr}} = \frac{mc^2}{4\ln 2 k {\nu_0}^2} \left(\frac{1}{\alpha} \Delta \nu_{D\_\mathrm{XBSAS}} \right)^2 . \tag{5.13}$$

5.4 Uncertainty Analysis of XBSAS

The differential of Equation (5.13) yields

$$\frac{\Delta T_{\mathrm{tr}}}{T_{\mathrm{tr}}} = 2\left\{ \frac{\Delta\alpha}{\alpha} + \frac{\Delta\left(\Delta\nu_{D\_\mathrm{XBSAS}}\right)}{\Delta\nu_{D\_\mathrm{XBSAS}}} \right\}. \tag{5.14}$$

XBSAS is performed at highly saturated region and the uncertainty of α is negligible. The relationship between FWHM and absorption coefficient is[50]

$$\frac{\Delta\left(\Delta\nu_{D\_\mathrm{XBSAS}}\right)}{\Delta\nu_{D\_\mathrm{XBSAS}}} \approx \frac{\Delta\left(k - k_{\mathrm{cs}}\right)}{k - k_{\mathrm{cs}}} \tag{5.15}$$

Equation (5.14) is rewritten as

$$\frac{\Delta T_{tr}}{T_{tr}} = 2\frac{\Delta(k - k_{cs})}{k - k_{cs}}. \tag{5.16}$$

From Equations (5.5) and (5.16),

$$\frac{\Delta T_{tr}}{T_{tr}} = 2\left\{\frac{\Delta(\Delta I)}{\Delta I} + \frac{\Delta I_{ps}}{I_{ps}}\right\}. \tag{5.17}$$

I_{ps} can be measured with uncertainty of less than 0.1 %. Thus the uncertainty in temperature measurement is determined by $\Delta(\Delta I)/\Delta I$, which depends on k-k_s and the uncertainty in the lock-in-amplifier. k-k_s is a function of k, Δx, I_{ps} and I/I_s.

$$\frac{\Delta T_{tr}}{T_{tr}} = 2\frac{\Delta(\Delta I)}{(k - k_{cs}(I/I_s))\Delta x I_{ps}} \tag{5.18}$$

The utilization of high intensity saturating beam is effective for accurate measurement. Although a large I_{ps} also improves the accuracy, I_{ps} has to be smaller than saturation intensity, I_s. Δx is determined by a desired spatial resolution. For simplicity, k-k_{cs} is approximated as

$$k - k_{cs}(I/I_s) = k'\left\{1 - \frac{1}{\sqrt{1 + (I/I_s)}}\right\}, \tag{5.19}$$

where k' is

$$k' = K_i \frac{\sqrt{\ln 2}}{\pi^{3/2}} \frac{\Delta\nu_L}{\Delta\nu_D} \int_{-\infty}^{\infty} \frac{\exp\left(-2\left(2\sqrt{\ln 2}\nu/\Delta\nu_D\right)^2\right) d\nu_\xi}{(\nu - \nu_\xi)^2 + (\Delta\nu_L/2)^2}. \tag{5.20}$$

Finally the uncertainty in temperature measurement is expressed as follows.

$$\frac{\Delta T_{tr}}{T_{tr}} = \frac{\Delta(\Delta I)}{k'\Delta x\left(1 - \frac{1}{\sqrt{1 + I/I_s}}\right) I_{ps}} \tag{5.21}$$

In our system $\Delta(\Delta I)/I_{ps}$ is in the order of 10^{-5}. Figure 5.7 shows the estimate uncertainty in temperature measurement as a function of I/I_s for different values of absorbance, $k'\Delta x$.

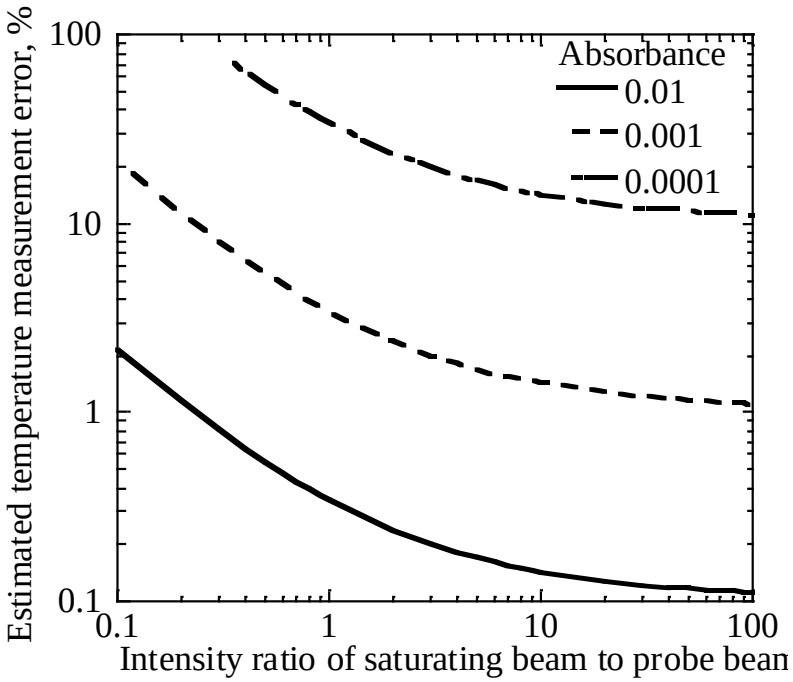

Figure 5.7 Estimated uncertainty of temperature.

5.5 Spatial Resolution of XBSAS

The alignment of two beams is important in the experimental setup of XBSAS. There are two important factors. One is the angle between two beams and the other is their beam diameters. When the angle between two beams substantially departs from right angle, the aforementioned description about XBSAS profile is not valid. In such case only the atoms with $\mathbf{v}= \{0, 0, v_z\}$ contribute to the saturated absorption and the Lamb Dip appears at the center of absorption. This is saturated absorption spectroscopy (or Doppler free spectroscopy).

Figure 5.8 shows the schematic of crossing two beams with an indication of spatial resolution. Once the saturating beam is prepared, the saturating beam power, P_s is fixed and its diameter, d_s can be adjusted with lenses. The saturating beam intensity, I is $4P_s/\pi d_s^2$. The XBSAS signal can be expressed as a function of d_s.

$$-\frac{\Delta I}{I_{ps}} = \left(k - k_{cs}\left(4P_s / \pi d_s^2\right)\right)d_s \tag{5.22}$$

Approximately,

$$-\frac{\Delta I}{I_{\mathrm{ps}}} = k' d_s \left(1 - 1/\sqrt{1 + 4P_s / \pi d_s^2 I_s}\right) \tag{5.23}$$

The spatial resolution is determined by d_s. When the saturating beam is focused on the crossing point, the spatial resolution becomes better and intensity increases. When it is defocused, the spatial resolution gets worse and intensity reduces. The example of XBSAS signal as a function of d_s is shown in Figure 5.9. In shock layer measurement the spatial resolution needs to be less than 1 mm. When the spatial resolution is set higher, the XBSAS signal gets lower.

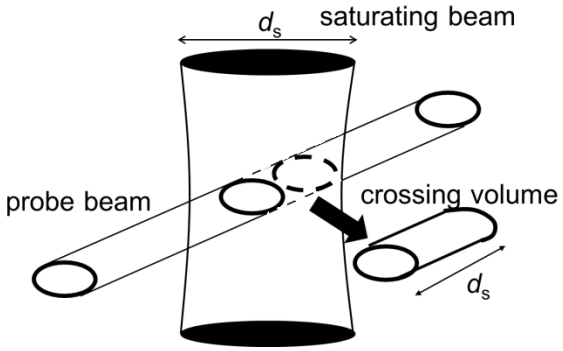

Figure 5.8 Schematic of crossing two beams.

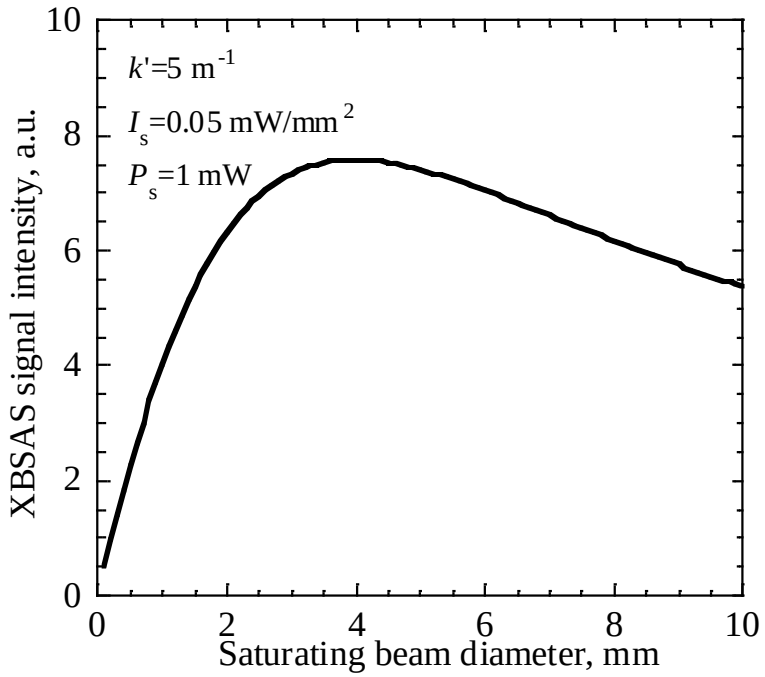

Figure 5.9 Signal intensity of XBSAS as a function of spatial resolution.

5.6 Experimental setup

5.6.1 Measurement system

Figure 5.10 shows the experimental setup. The main part of the setup is the same as what is shown in the previous chapter. The laser wavelength was swept at the repetitive frequency of 0.1 Hz with the sweeping width of 10 GHz so as not to be distorted by a low pass filter in the lock-in amplifier. The laser is divided into the saturating beam and others. The saturating beam was modulated with an acousto-optic modulator (AOM, 1205C; Isomet Corp.) and introduced into the optical fiber. The laser power at the output of the fiber is 1.0 mW and the laser spatial width at the measurement point was 0.8 mm at the crossing point. The fiber coupler is mounted at the upper side of chamber. The probe beam is coupled into the fiber and introduced to the chamber. The diameter is 0.8 mm at the crossing point and the power is 15 μW. The diameter of the laser is measured with beam profiler (SP503U; Ophir Optronics Solutions Ltd.). The evacuation of chamber may misalign the two beams. The probe beam was mounted on the optical table and was not displaced by the evacuation. The saturating beam was mounted on a flange. The flange moves down during the

evacuation because an o-ring between chamber and window is squashed. This displacement can be compensated by mounting the saturating beam near the window and by putting a load to make the displacement vertical. The transmitted probe beam is divided into two beams. One is detected by PD2 (DET100; Thorlab Inc.)as a reference signal. This signal gives LAS result and is used for the evaluation of the line-integrated absorption signal. The other is detected by PD1 and the output of it is connected with a lock-in amplifier (LIA, SR830; Stanford Research Systems Inc.). This is for XBSAS. The triangle wave signal for AOM controller is used as a reference of LIA. The output of LIA is recorded with the oscilloscope.

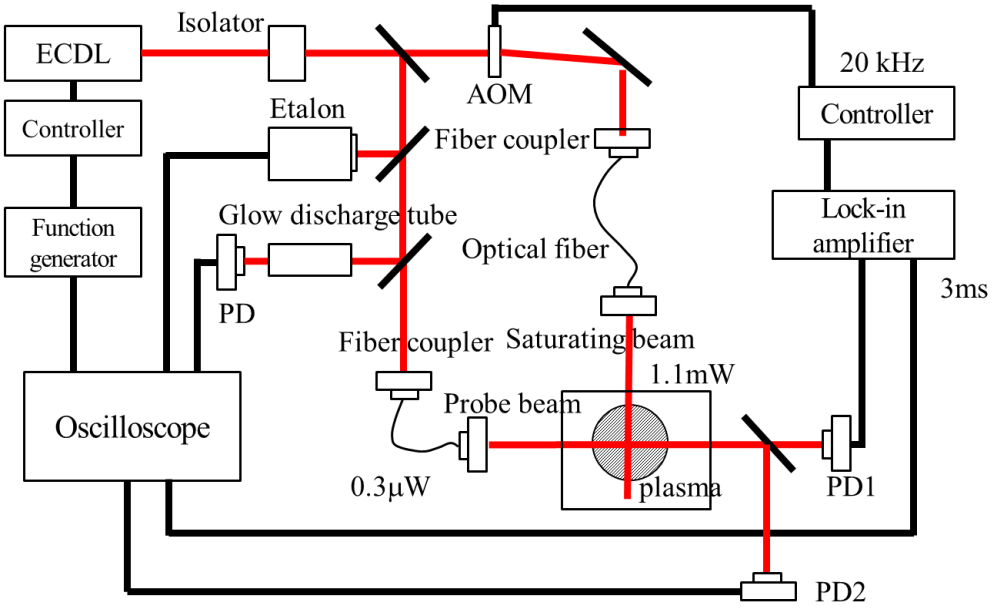

Figure 5.10 Experimental setup of XBSAS.

5.6.2 Generation of a plasma flow and shock layer

The arc-heated plasma generator was the same as the one which is shown in Chapter 4. The shock layer was generated with a spherical probe made of brass, diameter of which was 25.4 mm. The probe was water-cooled and moved with a stepping motor. The measurement point was fixed at 30 mm away from the nozzle exit. Figure 5.11 is the photograph of the probe in the flow. The laser diameter was 0.8 mm at the crossing point. The refraction effect of laser beam at the shock wave is negligibly small, and the alignment of two beams was not affected by the shock wave. The plenum and chamber pressures were respectively about 50 kPa and 20 Pa. This indicates the flow is

under-expansion flow. Mach number of the flow was deduced as 2.27±0.26 by LAS using Equation (4.6) with γ=5/3 and R=207 J/kgK, while the designed Mach number is 2.

$$M = \frac{V}{\sqrt{\gamma R T_{\mathrm{tr}}}} \tag{5.24}$$

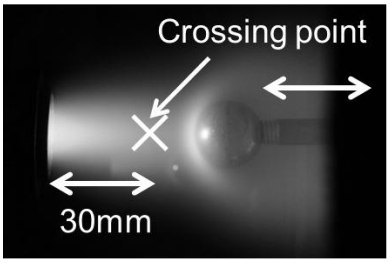

Figure 5.11 Photograph of the spherical probe in the flow.

Shock stand-off distance, Δd for a sphere probe was theoretically and experimentally estimated by several authors[108–110]. Figure 5.12 shows the coordinate system around the shock layer. According to Lobb's approximation, the ratio of Δd to the probe diameter, D is approximately related to the ratio of density in the free stream to behind the shock wave as following for non-reacting flow

$$\frac{\Delta d}{D} \cong 0.41\left(\frac{\rho_2}{\rho_1}\right)^{-1}, \tag{5.25}$$

where

$$\frac{\rho_2}{\rho_1} = \frac{(\gamma+1)M_1^2}{(\gamma-1)M_1^2+2}. \tag{5.26}$$

With M_1=2.27 and D=25.4 mm, Δd is estimated at 4 mm.

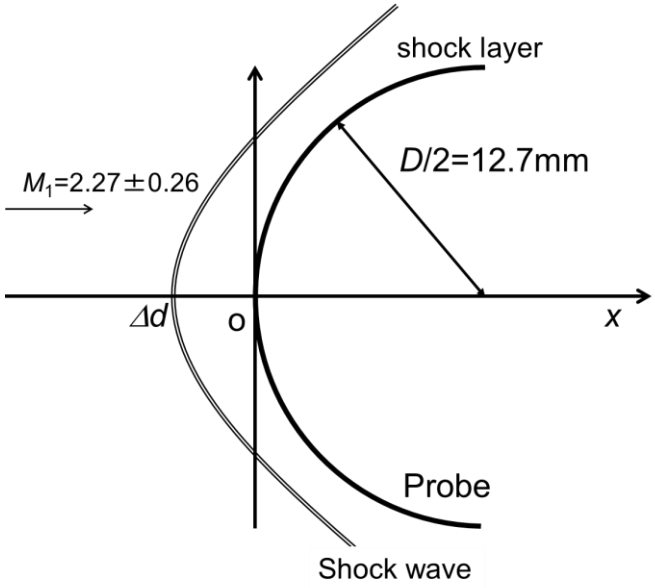

Figure 5.12 Coordinate for the shock layer over the spherical probe.

5.7 Results and discussions

5.7.1 Free stream measurement

First the saturation intensity was obtained as shown in Figure 5.13. By fitting, the saturation intensity was estimated at 0.063 mW.

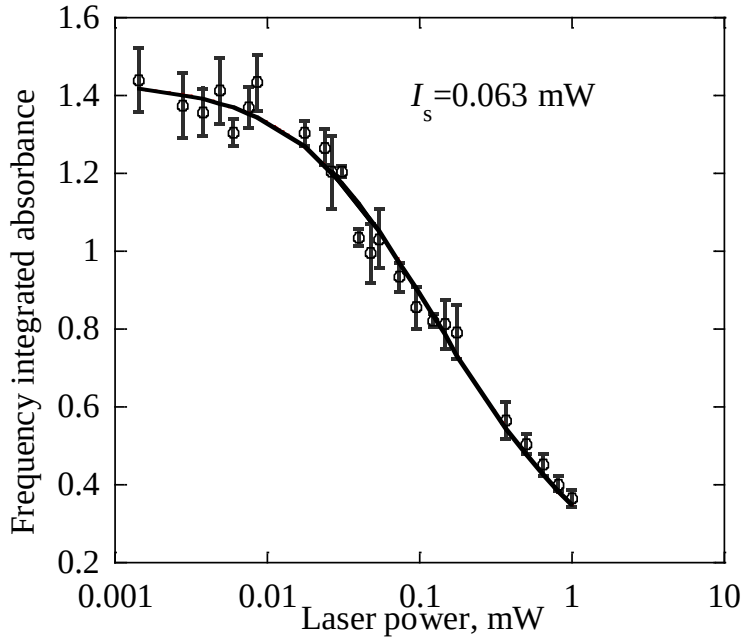

Figure 5.13 Saturated integrated absorbance as a function of laser power.

The signals of PD1, PD2 and etalon are shown in Figure 5.14. In XBSAS, fluorescence emits from the crossing point because of the high intensity saturating beam. The fluorescence detection must be avoided. There was no collecting lens in this optical setup and the detector was put away from the plasma to avoid the plasma emission. Thus, no fluorescence was detected during the measurement. This can be checked by blocking the probe beam. If the substantial signal is detected without the probe beam, its signal is LIF signal. In such case the pin hole is effective to avoid the fluorescence detection.

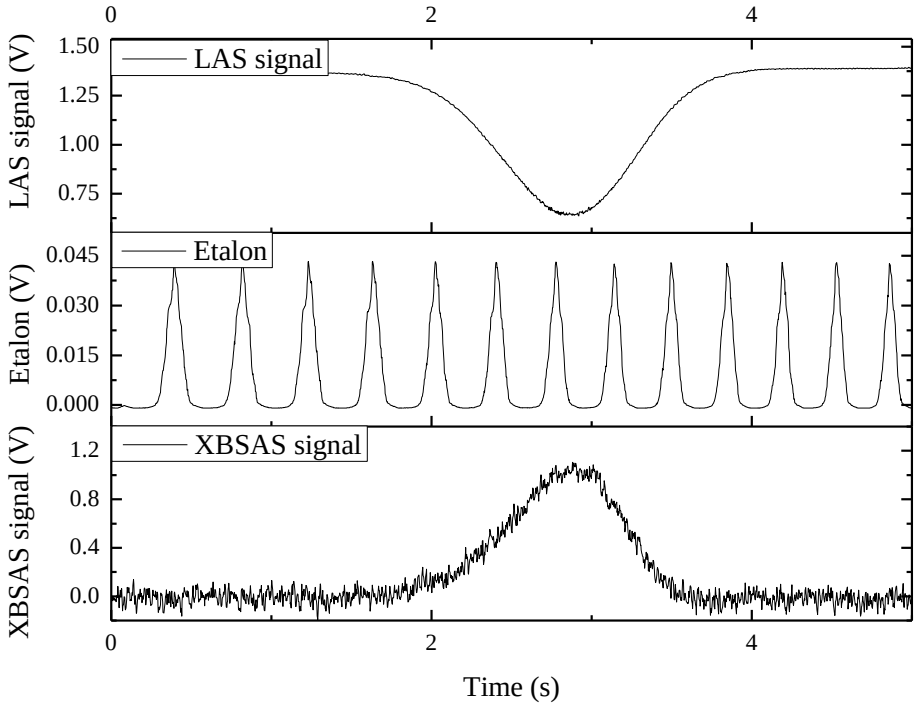

Figure 5.14 Signal of XBSAS (detected by PD1), etalon, and LAS (detected by PD2).

The difference between unsaturated and saturated absorption coefficient was calculated by Equation (5.4) as shown in Figure 5.15. The profile in Figure 5.15 was slightly asymmetric. This may come from the interpolation error of laser intensity in the absorption region. However, this asymmetry does not yield the substantial error in the temperature measurement.

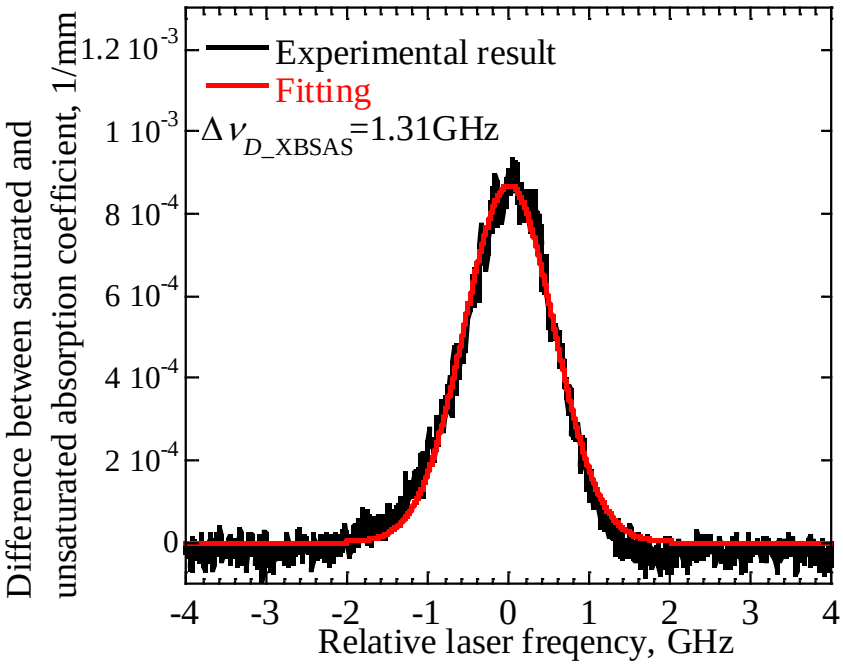

Figure 5.15 Typical signal of saturated absorption coefficient.

FWHM of XBSAS profile was deduced as 1.36 GHz by fitting with the Gaussian function. As shown in Figure 5.6 when the saturation parameter was 15, the ratio of FWHM of measured profile to true profile is 0.68. Therefore, FWHM of true profile and corresponding temperature were deduced as 2.00 GHz and 2070 K. With four times measurements, the mean translational temperature at the center was deduced as 2040 K. From Equation (5.21), the uncertainty of this measurement is about 3%, thus the temperature is evaluated as 2040±60 K. The result of LAS with Abel inversion is shown in Figure 5.16. Translational temperature at the flow center is 1940±100 K.. The result of XBSAS was in a good agreement with the result of LAS spatially resolved by Abel inversion.

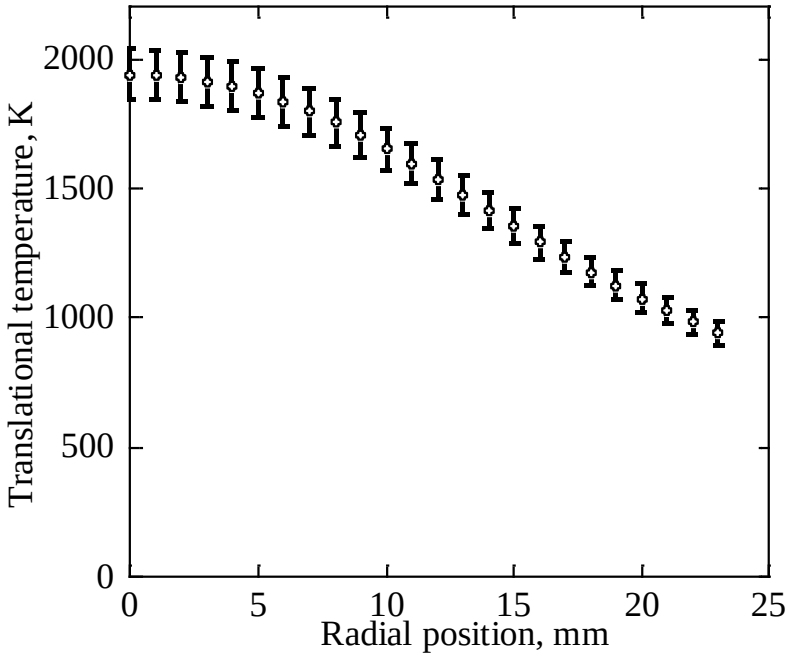

Figure 5.16 Radial distribution of translational temperature obtained by LAS.

Table 5.2 Translational temperature obtained by XBSAS and LAS.

XBSAS	LAS
2040±60 K	1940±100 K

5.7.2 Shock layer measurement

XBSAS was applied to the shock layer measurement. The translational temperature distribution along the stagnation streamline is shown in Figure 5.17. In this facility, the mean free pass, λ was about 2 mm, and the plasma flow is in the transition region from the continuous flow to free molecular flow (*Kn*=0.1~1). Thus the temperature jumped slowly from the free stream to the shock layer. The pressure behind the shock was estimated at 120 Pa by using following equation.

$$\frac{p_2}{p_1} = \frac{2\gamma M_1^2 - (\gamma - 1)}{\gamma + 1} \tag{5.27}$$

Although this pressure increase may alter the saturation intensity behind the shock, in the highly saturated region this effect can be ignored as shown in Figure 5.6. Therefore it is assumed that the saturation intensity doesn't vary in the field.

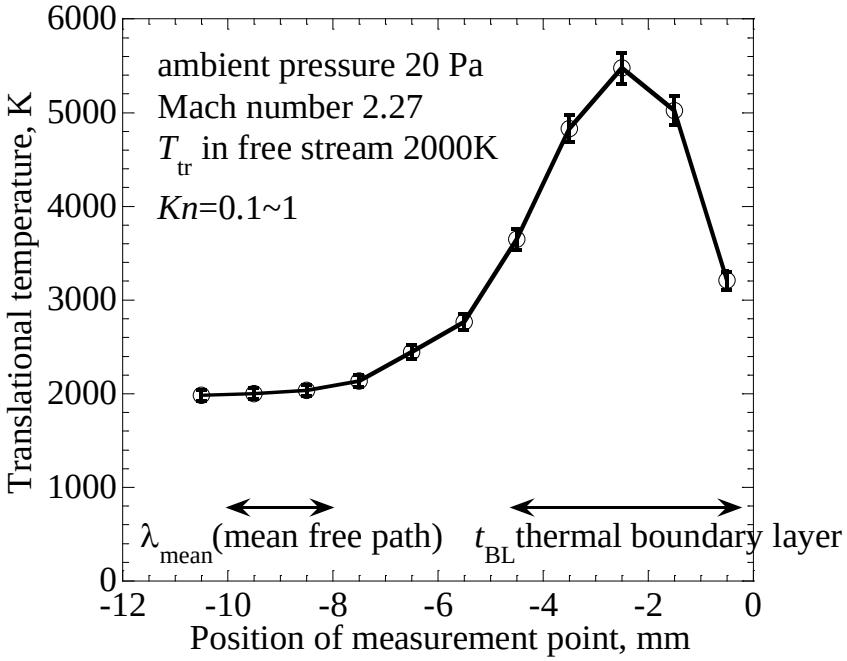

Figure 5.17 Axial distribution of translational temperature in front of the probe with scales of mean free path and thermal boundary layer.

Table 5.3 Translational temperature in the shock layer.

Measured and estimated temperature	Value
Measured peak temperature	5470 K
Estimated stagnation temperature	5400 K

The peak temperature was 5470±200 K at x=-2.5 mm. With the free stream temperature and Mach number, the stagnation temperature was estimated to be over 5400 K, and the temperature measured by XBSAS is in reasonable agreement with it. The specific enthalpy estimated by the energy balance method was 3.7 MJ/kg and the probe surface temperature and free stream temperature were respectively about 1200 K and 2000 K. Thus the thermal boundary layer was estimated at about 5 mm and merged with the shock wave. At x=-0.5 mm, the temperature deduced by line-integrated LAS was 3200±200 K, while the temperature deduced by XBSAS was 3200±20 K. It is considered that at this point the temperature was overestimated by LAS because of the convolution of blue shift and red shift in the absorption. Thus at x=-0.5 mm only XBSAS can deduce the translational

temperature. This is the first demonstration of translational temperature measurement in the shock layer. When other methods are developed in the future, this result can be validated.

5.8 Summary

Cross-beam saturated absorption spectroscopy (XBSAS) was developed for point measurements of translational temperature. First, the profile function of XBSAS was derived and the translational temperature was measured as 2040±60 K in the free stream of argon plasma. This result was in the good agreement with the result of LAS which was spatially resolved by Abel inversion. Next, XBSAS was applied to the merged shock layer measurement. The translational temperature distribution along stagnation streamline was obtained. At the peak the temperature was deduced as 5470±200 K, which showed the reasonable agreement with the stagnated temperature estimated from the free stream temperature and Mach number. XBSAS can be a powerful tool to resolve the temperature distribution in the shock layer, which has not been experimentally obtained before. By introducing a higher intensity laser as the saturating beam, the spatial resolution and measurement uncertainty can be improved.

Chapter 6 Conclusion

Applicability of laser absorption and laser-induced fluorescence spectroscopic measurements in plasma wind tunnels was extended for diagnosis of uncovered flow properties. 1) Application of cavity enhanced absorption spectroscopy (CEAS) to a 750 kW arc-heated plasma wind tunnel under undesired mechanical vibration, 2) correction of diode laser-induced fluorescence (DLIF) profile in optically thick plasma and 3) point measurement of translational temperature by cross-beam saturated absorption spectroscopy (XBSAS) have been achieved successfully with following remarks.

6.1 Absorption Measurement of Atomic Oxygen in a 750 kW Arc-heated Plasma Wind Tunnel by CEAS

The absorption measurement in an air plasma flow has never been achieved in any large-scale (0.1 to 1 MW) arc-heated wind tunnel in the world. In this thesis CEAS was successfully applied to the JAXA's 750 kW arc-heated plasma wind tunnel for the first time with following techniques.

6.1.1 Elimination of undesired resonance signals in data processing

At the large-scale plasma wind tunnel measurement, the optical cavity which is designed for the longitude mode resonance faces to the vibrating environment and the resonance signal on the transverse mode is induced. The elimination of undesigned resonance signal in the data processing improved the sensitivity. The minimum detectable absorbance in one sweep was 0.0014.

6.1.2 Averaging over 100 sweeps of laser wavelength

It was impossible to identify the absorption signal in one sweep of laser wavelength. A hundred sweeps were recorded and the absorption signal was successfully observed on the averaged profile.

The sensitivity was improved by two orders of magnitude and the minimum detectable absorbance of this system was 3.0×10^{-4}.

6.2 DLIF Spectroscopy in Optically Thick Plasma in Combination with Laser Absorption Spectroscopy

The distorted DLIF profile in optically thick plasma with an intense laser was corrected in

combination with LAS. The corrected broadening was 1.96±0.1 GHz, which corresponds to 1990±200 K, while the uncorrected broadening was 2.20±0.02 GHz.

6.2.1 Correction for Laser Absorption

The absorption of exciting laser broadens the fluorescence profile wider than the true profile. By monitoring the transmitted laser intensity, the absorption profile was corrected. With peak absorbance of 0.1, the temperature was overestimated by 2%. At high intensity this effect negligible because of the saturated absorption of exciting laser.

6.2.2 Correction for Saturation Broadening

Although the intense exciting laser has induces fluorescence with a high signal-to-noise ratio, the profile exhibits saturation broadening. The ratio of saturated broadening to unsaturated broadening was obtained by performing LAS with varying probe laser intensity. The overestimated broadening was corrected with this ratio. Saturation broadening led to 16% higher temperature than true temperature.

6.2.3 Correction for Fluorescence Re-absorption

The re-absorption of fluorescence broadened the profile. By performing unsaturated LAS with low intensity laser, this effect was corrected. The temperature was overestimated by 8% because of this effect.

6.3 Development of XBSAS for Translational Temperature Measurement in Shock Layer

Cross-beam saturated absorption spectroscopy (XBSAS) was developed for translational temperature measurements. With this novel technique translational temperature distribution along the stagnation streamline in the shock layer can be obtained. This distribution can be helpful information to deepen the knowledge about wall catalytic recombination, internal energy relaxation, and shock layer structure and for validation of numerical simulations. Furthermore, this novel technique is applicable to plasma diagnosis in other fields, such as electric propulsion and chemical vapor deposition.

6.3.1 Derivation of line shape function of XBSAS profile

The line shape function of XBSAS was derived and the XBSAS profile in the free stream was evaluated. The deduced temperature showed the good agreement with the LAS result which was

spatially resolved by Abel inversion.

6.3.2 Distribution of translational temperature on a stagnation streamline

The distribution of translational temperature on the stagnation streamline was obtained across the shock wave which was generated with 25 mm sphere. The temperature started to increase around 6 mm in front of the probe then decreased toward the probe. The peak temperature showed the reasonable agreement with the estimated stagnation temperature.

Lastly the applicability of laser diagnostics based on LAS and LIF for high enthalpy flow was extended.

References

[1] Byron, S. R., "Measurement of the Rate of Dissociation of Oxygen," *The Journal of Chemical Physics*, vol. 30, 1959, pp. 1380–1392.

[2] Byron, S., "Shock-Tube Measurement of the Rate of Dissociation of Nitrogen," *The Journal of Chemical Physics*, vol. 44, 1966, pp. 1378–1388.

[3] Itoh, K., Ueda, S., Tanno, H., Komuro, T., and Sato, K., "Hypersonic aerothermodynamic and scramjet research using high enthalpy shock tunnel," *Shock Waves*, vol. 12, Aug. 2002, pp. 93–98.

[4] Sahoo, N., Mahapatra, D. R., Jagadeesh, G., Gopalakrishnan, S., and Reddy, K. P. J., "An accelerometer balance system for measurement of aerodynamic force coefficients over blunt bodies in a hypersonic shock tunnel," *Measurement Science and Technology*, vol. 14, 2003, pp. 260–272.

[5] Park, C., *User's Manual:Nonequilibrium Air Radiation (NEQAIR) Program*, 1985.

[6] Whiting, E. E., Park, C., Liu, Y., Arnold, J. ., and Paterson, J. ., *NEQAIR96, Nonequilibrium and Equilibrium Radiative Transport and Spectra Program: User's Manual*, 1996.

[7] Fujita, K., and Takashi, A., *SPRADIAN, Structured Package for Radiation Analysis:Theory and Application*, 1997.

[8] Fujita, K., Mizuno, M., Ishida, K., and Ito, T., "Spectroscopic Flow Evaluation in Inductively Coupled Plasma Wind Tunnel," *Journal of Thermophysics and Heat Transfer*, vol. 22, Oct. 2008, pp. 685–694.

[9] Hyun, S.-Y., "Radiation code SPRADIAN07 and its application," 2009.

[10] Hyun, S.-Y., Park, C., and Chang, K.-S., "Rate Parameters for Electronic Excitation of Diatomic Molecules: NO Radiation," *Journal of Thermophysics and Heat Transfer*, vol. 23, Oct. 2009, pp. 641–650.

[11] Hyun, S.-Y., Park, C., and Chang, K.-S., "Rate Parameters for Electronic Excitation of Diatomic Molecules: CN Radiation," *Journal of Thermophysics and Heat Transfer*, vol. 23, Apr. 2009, pp. 226–235.

[12] Pfeiffer, B., Fertig, M., Winter, M., and Auweter-Kurtz, M., "PARADE-a program to calculate the radiation of atmospheric re-entry in different atmospheres," *First International Workshop on Radiation of High Temperature Gases in Atmospheric Entry*, 2003, pp. 85–99.

[13] Fujita, K., Sato, S., and Abe, T., "Experimental Investigation of Air Radiation from Behind a Strong Shock Wave Introduction," *Journal of Thermophysics and Heat Transfer*, vol. 16, 2002, pp. 3–8.

[14] Takama, Y., and Suzuki, K., "Spectroscopic Observation of Translational–Rotational Nonequilibrium in Low-Density Hydrogen Plasma Flow," *Journal of Thermophysics and Heat Transfer*, vol. 23, Jul. 2009, pp. 454–462.

[15] Cohent, L. M., and Hanson, R. K., "Emission and laser-induced fluorescence measurements in a supersonic jet of plasma-heated nitrogen," *Journal of Physics D: Applied Physics*, vol. 25, 1992, pp. 339–351.

[16] Mizuno, M., Ishida, K., Ito, T., Kurotaki, T., and Matsuzaki, T., "Oxygen Recombination Coefficient on Catalytic Surfaces in Ar-O2 Inductively Coupled Plasma by Actinometry," *Transactions of the Japan Society for Aeronautical and Space Sciences*, vol. 49, 2006, pp. 49–54.

[17] Kihara, H., Hatano, M., Nakiyama, N., Abe, K., and Nishida, M., "Preliminary Studies of Spallation Particles Ejected from an Ablator," *Transactions of the Japan Society for Aeronautical and Space Sciences*, vol. 49, 2006, pp. 65–70.

[18] Hirakawa, M., Abe, K.-I., Nishida, M., Takeishi, K., and Matsuura, M., "Application of a 20 kW Arc-Heated Wind Tunnel to Evaluation Tests of Wall Catalysis," *Trans. JSASS Aerospace Tech. Japan*, vol. 45, 2003, pp. 217–223.

[19] Park, C., "Assessment of two-temperature kinetic model for ionizing air," *Journal of Thermophysics and Heat Transfer*, vol. 3, Jul. 1989, pp. 233–244.

[20] Filippis, F. De, Purpura, C., Viviani, A., Acampora, L., and Fusco, M., "Chemical Species and Nonequilibrium Temperatures for Airflows in a Plasma Wind Tunnel," *Journal of Thermophysics and Heat Transfer*, vol. 24, Apr. 2010, pp. 271–280.

[21] Marschall, J., and Fletcher, D. G., "High-enthalpy test environments, flow modeling and in situ diagnostics for characterizing ultra-high temperature ceramics," *Journal of the European Ceramic Society*, vol. 30, Aug. 2010, pp. 2323–2336.

[22] Matsui, M., Komurasaki, K., Arakawa, Y., Knapp, A., Herdrich, G., and Auweter-Kurtz, M., "Enthalpy Measurement of Inductively Heated Airflow," *Journal of Spacecraft and Rockets*, vol. 45, Jan. 2008, pp. 155–158.

[23] Matsui, M., Takayanagi, H., Oda, Y., Komurasaki, K., and Arakawa, Y., "Performance of arcjet-type atomic-oxygen generator by laser absorption spectroscopy and CFD analysis," *Vacuum*, vol. 73, Apr. 2004, pp. 341–346.

[24] Nomura, S., Komurasaki, K., and Arakawa, Y., "Measurement of Specific Heat Ratio of an Arc-Heater Plume," *Applied Plasma Science*, vol. 16, 2008, pp. 157–161.

[25] Nomura, S., Komurasaki, K., Loehle, S., and Herdrich, G., "Evaluation of Nonequilibrium Excitation of Inductively Heated Atomic Oxygen by Laser Absorption Spectroscopy," *Frontier of Applied Plasma Technology*, vol. 4, 2011, pp. 65–69.

[26] Kim, S., "Development of Tunable Diode Laser Absorption Sensors for A Large-Scale Arc-Heated-Plasma Wind Tunnel," Stanford University, 2004.

[27] Mohamed, a, Rosier, B., Sagnier, P., Henry, D., Louvet, Y., and Bize, D., "Application of infrared diode laser absorption spectroscopy to the F4 high enthalpy wind tunnel," *Aerospace Science and Technology*, vol. 2, May. 1998, pp. 241–250.

[28] Matsui, M., and Komurasaki, K., "Enthalpy Measurement in Inductively Heated Plasma Generator," *AIAA Journal*, vol. 43, 2005, pp. 8–12.

[29] Fletcher, D. G., "Arcjet flow properties determined from laser-induced fluorescence of atomic nitrogen.," *Applied optics*, vol. 38, Mar. 1999, pp. 1850–1858.

[30] Vecchio, A. Del, and Palumbo, G., "Temperature Measurements by Laser-Induced Fluorescence Spectroscopy in Nonequilibrium High-Enthalpy Flow," *Journal of thermophysics and heat transfer*, vol. 14, 2000, pp. 216–225.

[31] Löhle, S., Eichhorn, C., Steinbeck, A., Lein, S., Herdrich, G., Röser, H.-P., and Auweter-Kurtz, M., "Oxygen plasma flow properties deduced from laser-induced fluorescence and probe measurements.," *Applied optics*, vol. 47, Apr. 2008, pp. 1837–1845.

[32] Takayanagi, H., Mizuno, M., Fujii, K., Suzuki, T., and Fujita, K., "Arc Wind Tunnel Flow Characterization Measured by Laser-Induced Fluorescence of Atomic Species," *41th AIAA Thermophysics Conference*, 2009.

[33] Goehlich, a., Kawetzki, T., and Döbele, H. F., "On absolute calibration with xenon of laser diagnostic methods based on two-photon absorption," *The Journal of Chemical Physics*, vol. 108, 1998, pp. 9362–9370.

[34] Löhle, S., and Auweter-Kurtz, M., "Inductively Heated Air Plasma Flow Characterization with Laser-Induced Fluorescence Measurements," *Journal of Thermophysics and Heat Transfer*, vol. 23, Jan. 2009, pp. 208–210.

[35] Yamada, T., and Inatani, Y., "Nonequilibrium Temperatures Measurement in an Arc-Heated Airflow by the Optical Diagnostic Method," *Trans. JSASS Aerospace Tech. Japan*, vol. 45, 2002, pp. 83–93.

[36] Laufer, G., McKenzie, R. L., and Fletcher, D. G., "Method for measuring temperatures and densities in hypersonic wind tunnel air flows using laser-induced O2 fluorescence.," *Applied optics*, vol. 29, Nov. 1990, pp. 4873–4883.

[37] Boubert, P., Chaix, a., Chikhaoui, a., Robin, L., and Vervisch, P., "Aerodynamic calibration of TCM2 facility and study of a bow shock layer by emission and laser spectroscopy," *Shock Waves*, vol. 11, Apr. 2002, pp. 341–351.

[38] Babou, Y., Rivière, P., Perrin, M.-Y., and Soufiani, A., "Spectroscopic data for the prediction of radiative transfer in CO2–N2 plasmas," *Journal of Quantitative Spectroscopy and Radiative Transfer*, vol. 110, Jan. 2009, pp. 89–108.

[39] Bugel, M., Reynier, P., and Smith, A., "Survey of European and Major ISC Facilities for Supporting Mars and Sample Return Mission Aerothermodynamics and Tests Required for Thermal Protection System and Dynamic Stability," *International Journal of Aerospace Engineering*, vol. 2011, 2011, pp. 1–18.

[40] Kitagawa, K., Goto, H., Yasuhara, M., Kobayashi, Y., and Sakai, T., "Emission Spectra measuerments in the arc heated flow of Huels type arc heater," *15th AIAA International Space Planes and Hypersonic Systems and Technologies Conference*, 2008.

[41] Herdrich, G., and Marynowski, T., "Mars and Venus Entry Simulation Capabilities of IRS Plasma Wind Tunnel PWK3," *Applied Physics Research*, vol. 4, Jan. 2012, pp. 146–155.

[42] Guelhan, A., Esser, B., Koch, U., and Hannemann, K., "Mars Entry Simulation in the Arc Heated Facility L2K," *4th Europ Symp. Aerothermodynamics for Space Applications*, 2002, pp. 665–672.

[43] Marieu, V., Reynier, P., Marraffa, L., Vennemann, D., De Filippis, F., and Caristia, S., "Evaluation of SCIROCCO plasma wind-tunnel capabilities for entry simulations in CO2 atmospheres," *Acta Astronautica*, vol. 61, Oct. 2007, pp. 604–616.

[44] Lago, V., Lebehot, A., and Dudeck, M., "Entry conditions in planetary atmospheres: Emission spectroscopy of molecular plasma arcjets," *Journal of Thermophysics and Heat Transfer*, vol. 15, 2001, pp. 168–175.

[45] Splinter, S. C., Bey, K. M., and Gragg, J. G., "Comparative Measurements of Earth and Martian Entry Environments in the NASA Langley HYMETS Facility," *49th AIAA Aerospace Sciences Meeting including the New Horizons Forum and Aerospace Exposition2*, 2011.

[46] Rond, C., Bultel, a., Boubert, P., and Chéron, B. G., "Spectroscopic measurements of nonequilibrium CO2 plasma in RF torch," *Chemical Physics*, vol. 354, Dec. 2008, pp. 16–26.

[47] Mazouffre, S., and Pawelec, E., "Metastable oxygen atom velocity and temperature in supersonic CO 2 plasma expansions," *Journal of Physics D: Applied Physics*, vol. 42, Jan. 2009, p. 015203.

[48] Playez, M., and Fletcher, D. G., "Spectroscopic Analysis of Titan Atmospheric Plasmas," *Journal of Thermophysics and Heat Transfer*, vol. 22, Apr. 2008, pp. 150–156.

[49] Brandis, A. M., Morgan, R. G., McIntyre, T. J., and Jacobs, P. a., "Nonequilibrium Radiation Intensity Measurements in Simulated Titan Atmospheres," *Journal of Thermophysics and Heat Transfer*, vol. 24, Apr. 2010, pp. 291–300.

[50] Matsui, M., "Application of Laser Absorption Spectroscopy to High Enthalpy Flow Diagnostics," University of Tokyo, 2005.

[51] Demtroeder, W., *Laser Spectroscopy*, Springer-Verlag, 2002.

[52] Végh, J., "Alternative form for the pseudo-Voigt peak shape," *Review of Scientific Instruments*, vol. 76, 2005, p. 056107.

[53] Ida, T., Ando, M., and Toraya, H., "Extended pseudo-Voigt function for approximating the Voigt profile," *Applied Crystallography*, vol. 33, 2000, pp. 1311–1316.

[54] Humlicek, J., "Optimized computation of the voigt and complex probability functions," *Journal of Quantitative Spectroscopy and Radiative Transfer*, vol. 27, 1982, pp. 437–444.

[55] Hui, A. K., Armstrong, B. H., and Wray, A. A., “RAPID COMPUTATION OF THE VOIGT AND COMPLEX,” *Journal of Quantitative Spectroscopy and Radiative Transfer*, vol. 19, 1978, pp. 509–516.

[56] Daily, J. W., “Saturation effects in laser induced fluorescence spectroscopy,” *Applied optics*, vol. 16, 1977, pp. 568–571.

[57] OKeefe, A., and Deacon, D., “Cavity ring-down optical spectrometer for absorption measurements using pulsed laser sources,” *Review of Scientific Instruments*, vol. 59, 1988, pp. 2544–2552.

[58] Romanini, D., and Kachanov, A., “CW cavity ring down spectroscopy,” *Chemical physics letters*, vol. 264, 1997, pp. 316–322.

[59] Engeln, R., Berden, G., Peeters, R., and Meijer, G., “Cavity enhanced absorption and cavity enhanced magnetic rotation spectroscopy,” *Review of Scientific Instruments*, vol. 69, 1998, pp. 3763–3769.

[60] Hall, J. L., Ma, L., Ye, J., and Dube, P., “Ultrasensitive frequency-modulation spectroscopy enhanced by a high-finesse optical cavity : theory and application to overtone transitions of C 2 H 2 and C 2 HD,” *Journal of the Optical Society of America B*, vol. 16, 1999, pp. 2255–2268.

[61] Schmidt, F. M., Foltynowicz, A., Ma, W., Lock, T., and Axner, O., “Doppler-broadened fiber-laser-based NICE-OHMS – Improved detectability,” *Optics express*, vol. 15, 2007, pp. 10822–10831.

[62] Bomse, D. S., Stanton, a C., and Silver, J. a, “Frequency modulation and wavelength modulation spectroscopies: comparison of experimental methods using a lead-salt diode laser.,” *Applied optics*, vol. 31, Feb. 1992, pp. 718–731.

[63] Beckwith, P., and Brown, C., “High sensitivity detection of transient infrared absorption using tunable diode lasers,” *Applied optics*, vol. 26, 1987, pp. 2643–2649.

[64] Friedrichs, G., “Sensitive Absorption Methods for Quantitative Gas Phase Kinetic Measurements. Part 2: Cavity Ringdown Spectroscopy,” *Zeitschrift für Physikalische Chemie*, vol. 222, Jan. 2008, pp. 31–61.

[65] Morville, J., Romanini, D., Kachanov, A. a., and Chenevier, M., “Two schemes for trace detection using cavity ringdown spectroscopy,” *Applied Physics B: Lasers and Optics*, vol. 78, Feb. 2004, pp. 465–476.

[66] Maisons, G., Gorrotxategi Carbajo, P., Carras, M., and Romanini, D., “Optical-feedback cavity-enhanced absorption spectroscopy with a quantum cascade laser.,” *Optics letters*, vol. 35, Nov. 2010, pp. 3607–3609.

[67] Drever, R. W. P., Hall, J. L., Kowalski, F. V., Hough, J., Ford, G. M., Munley, a. J., and Ward, H., “Laser phase and frequency stabilization using an optical resonator,” *Applied Physics B Photophysics and Laser Chemistry*, vol. 31, Jun. 1983, pp. 97–105.

[68] Black, E. D., “An introduction to Pound–Drever–Hall laser frequency stabilization,” *American Journal of Physics*, vol. 69, 2001, pp. 79–87.

[69] Anderson, D. Z., “Alignment of resonant optical cavities.,” *Applied optics*, vol. 23, Sep. 1984, pp. 2944–2948.

[70] Li, Z., Stedman, G. E., and Bilger, H. R., “Asymmetric response profile of a scanning Fabry-Pérot interferometer,” *Optics Communications*, vol. 100, Jul. 1993, pp. 240–246.

[71] Bretenaker, F., Vallet, M., and Floch, A. Le, “Analytical and experimental study of ringing effects in a Fabry-Perot cavity. Application to the measurement of high finesses,” *Journal of the Optical Society of America B*, vol. 14, 1997, pp. 2811–2817.

[72] An, K., Yang, C., Dasari, R. R., and Feld, M. S., “Cavity ring-down technique and its application to the measurement of ultraslow velocities.,” *Optics letters*, vol. 20, May. 1995, p. 1068.

[73] Mazurenka, M., Orr-Ewing, A. J., Peverall, R., and Ritchie, G. a. D., “4 Cavity ring-down and cavity enhanced spectroscopy using diode lasers,” *Annual Reports Section “C” (Physical Chemistry)*, vol. 101, 2005, pp. 100–142.

[74] Hahn, J. W., Yoo, Y. S., Lee, J. Y., Kim, J. W., and Lee, H. W., “Cavity ringdown spectroscopy with a continuous-wave laser: calculation of coupling efficiency and a new spectrometer design.,” *Applied optics*, vol. 38, Mar. 1999, pp. 1859–1866.

[75] Matsui, M., Komurasaki, K., Ogawa, S., and Arakawa, Y., “Influence of laser intensity on absorption line broadening in laser absorption spectroscopy,” *Journal of Applied Physics*, vol. 100, 2006, p. 063102.

[76] Matsui, M., Ikemoto, T., Takayanagi, H., Komurasaki, K., and Arakawa, Y., “Generation of Highly Dissociated Oxygen Flows Using a Constrictor-Type Arc Heater,” *Journal of Thermophysics and Heat Transfer*, vol. 21, Jan. 2007, pp. 246–249.

[77] Scott, C., “Survey of measurements of flow properties in arc jets,” *Journal of Thermophysics and Heat Transfer*, vol. 7, 1990, pp. 9–24.

[78] Park, C., Raiche, G. a., Driver, D. M., Olejniczak, J., Terrazas-Salinas, I., Hightower, T. M., and Sakai, T., “Comparison of Enthalpy Determination Methods for an Arc-Jet Facility,” *Journal of Thermophysics and Heat Transfer*, vol. 20, Oct. 2006, pp. 672–679.

[79] Matsuzaki, T., Ishida, K., Watanabe, Y., Miho, K., Itagaki, H., and Yoshinaka, T., *Construction and Characteristics of the 750kW Arc Heated Wind Tunnel*, 2001.

[80] Takayangi, H., “Application of High-Sensitive Laser Absorption Spectroscopy to High Enthalpy Flow Diagnostics,” 2007.

[81] Boivin, R. F., and Scime, E. E., “Laser induced fluorescence in Ar and He plasmas with a tunable diode laser,” *Review of Scientific Instruments*, vol. 74, 2003, pp. 4352–4360.

[82] Severn, G. D., Edrich, D. a., and McWilliams, R., “Argon ion laser-induced fluorescence with diode lasers,” *Review of Scientific Instruments*, vol. 69, 1998, pp. 10–15.

[83] Severn, G. D., Wang, X., Ko, E., Hershkowitz, N., Turner, M. M., and McWilliams, R., "Ion flow and sheath physics studies in multiple ion species plasmas using diode laser based laser-induced fluorescence," *Thin Solid Films*, vol. 506-507, May. 2006, pp. 674–678.

[84] Galbács, G., Galbács, Z., Axner, O., and Geretovszky, Z., "Assessment and application of diode laser induced fluorescence spectrometry in an inductively coupled plasma to the determination of lithium," *Spectrochimica Acta Part B: Atomic Spectroscopy*, vol. 60, Mar. 2005, pp. 299–306.

[85] Keesee, A. M., Scime, E. E., and Boivin, R. F., "Laser-induced fluorescence measurements of three plasma species with a tunable diode laser," *Review of Scientific Instruments*, vol. 75, 2004, pp. 4091–4093.

[86] Cleary, P. a, Wooldridge, P. J., and Cohen, R. C., "Laser-induced fluorescence detection of atmospheric NO2 with a commercial diode laser and a supersonic expansion.," *Applied optics*, vol. 41, Nov. 2002, pp. 6950–6956.

[87] Severn, G., Wang, X., Ko, E., and Hershkowitz, N., "Experimental Studies of the Bohm Criterion in a Two-Ion-Species Plasma Using Laser-Induced Fluorescence," *Physical Review Letters*, vol. 90, Apr. 2003, pp. 145001–1–145001–4.

[88] Oksuz, L., Khedr, M. A., and Hershkowitz, N., "Laser induced fluorescence of argon ions in a plasma presheath," *Physics of Plasmas*, vol. 8, 2001, pp. 1729–1733.

[89] Hertz, H. M., and Aldén, M., "Calibration of imaging laser-induced fluorescence measurements in highly absorbing flames," *Applied Physics B Photophysics and Laser Chemistry*, vol. 42, Feb. 1987, pp. 97–102.

[90] Vidal, F., Laville, S., Goueguel, C., Loudyi, H., Rifai, K., Chaker, M., and Sabsabi, M., "A simple model of laser-induced fluorescence under arbitrary optical thickness conditions at the excitation wavelength," *Journal of Quantitative Spectroscopy and Radiative Transfer*, vol. 111, Nov. 2010, pp. 2528–2533.

[91] Liebeskind, J. G., Hanson, R. K., and Cappelli, M. a, "Laser-induced fluorescence diagnostic for temperature and velocity measurements in a hydrogen arcjet plume.," *Applied optics*, vol. 32, Oct. 1993, pp. 6117–6127.

[92] Goeckner, M. J., Goree, J., and Sheridan, T. E., "Saturation broadening of laser-induced fluorescence from plasma ions," *Review of Scientific Instruments*, vol. 64, 1993, pp. 996–1000.

[93] Takubo, Y., Yano, H., Matsuoka, H., and Shimazu, M., "Saturation behavior of laser-induced CH fluorescence in a propane-air flame," *Journal of Quantitative Spectroscopy and Radiative Transfer*, vol. 30, Aug. 1983, pp. 163–168.

[94] Omenetto, N., Benetti, P., and Hart, L., "Non-linear optical behavior in atomic fluorescence flame spectrometry," *Spectrochimica Acta*, vol. 28, 1973, pp. 289–300.

[95] Daily, J. W., "Saturation of fluorescence in flames with a Gaussian laser beam.," *Applied optics*, vol. 17, Jan. 1978, pp. 225–229.

[96] Alkemade, C., “Anomalous saturation curves in laser-induced fluorescence,” *Spectrochimica Acta Part B: Atomic Spectroscopy*, vol. 40, 1985, pp. 1331–1368.

[97] Goeckner, M. J., and Goree, J., “Laser-induced fluorescence measurement of plasma ion temperatures: Corrections for power saturation,” *Journal of Vacuum Science & Technology A: Vacuum, Surfaces, and Films*, vol. 7, May. 1989, pp. 977–981.

[98] Levine, J., “A simplified calculation of power-broadened linewidths, with application to resonance ionization mass spectrometry,” *Spectrochimica Acta Part B: Atomic Spectroscopy*, vol. 69, Mar. 2012, pp. 61–66.

[99] Goldsmith, J. E., “Spatially resolved saturated absorption spectroscopy in flames.,” *Optics letters*, vol. 6, Nov. 1981, pp. 525–527.

[100] Zizak, G., “Cross-beam polarization in flames with a pulsed dye laser,” *Applied optics*, vol. 25, 1986, pp. 3242–3246.

[101] Zizak, G., “Cross-beam saturated interference spectroscopy in flames,” *Applied optics*, vol. 24, 1985, pp. 3319–3321.

[102] Goldsmith, J. E., and Farrow, R. L., “Spatially resolved optical Stark-modulation spectroscopy in flames.,” *Optics letters*, vol. 7, May. 1982, pp. 215–217.

[103] Farrow, R. L., and Rahn, L. a, “Spatially resolved infrared absorption measurements: application of an optical Stark effect.,” *Optics letters*, vol. 6, Mar. 1981, pp. 108–110.

[104] Zizak, G., “Spatially resolved saturated absorption measurements of OH in methane-air flames,” *Applied optics*, vol. 26, 1987, pp. 4293–4297.

[105] Kychakoff, G., Howe, R. D., and Hanson, R. K., “Spatially resolved combustion measurements using cross-beam saturated absorption spectroscopy.,” *Applied optics*, vol. 23, May. 1984, pp. 1303–1305.

[106] Walters, P. E., Lanauze, J., and Winefordner, J. D., “Spatially resolved concentration studies of ground state atoms in a flame: saturated absorption spectroscopic method,” *Spectrochimica Acta Part B*, vol. 39B, 1984, pp. 125–129.

[107] Walters, P. E., “Spatially resolved concentration studies of ground state atoms and ions in an ICP: saturated absorption spectroscopic method,” *Spectrochimica Acta*, vol. 39, 1984, pp. 69–76.

[108] Olivier, H., “A theoretical model for the shock stand-off distance in frozen and equilibrium flows,” *Journal of Fluid Mechanics*, vol. 413, Jun. 2000, pp. 345–353.

[109] Hida, K., “An approximate study on the detached shock wave in front of a circular cylinder and a sphere,” *Journal of the Physical Society of Japan*, vol. 8, 1953, pp. 740–745.

[110] Olivier, H., “Influence of the velocity gradient on the stagnation point heating in hypersonic flow,” *Shock Waves*, vol. 5, Dec. 1995, pp. 205–216.